R and D CENTER LABORATORY

TECHNICAL REPORT

NO. TR12595

HOLOGRAPHIC ANALYSIS OF LARGE VEHICLE STRUCTURES

JULY 1982

by GRANT R. GERHART
GREGORY ARUTUNIAN
JAMES M. GRAZIANO

Approved for public release:
Distribution unlimited.

U.S. ARMY TANK-AUTOMOTIVE COMMAND
RESEARCH AND DEVELOPMENT CENTER
Warren, Michigan 48090

The citation of commercial products in this report does not constitute an official indorsement or approval of such products.

The findings in this report are not to be construed as an official Department of the Army position, unless so designated by other authorized documents.

UNCLASSIFIED

SECURITY CLASSIFICATION OF THIS PAGE *(When Data Entered)*

REPORT DOCUMENTATION PAGE		READ INSTRUCTIONS BEFORE COMPLETING FORM
1. REPORT NUMBER TR12595	2. GOVT ACCESSION NO.	3. RECIPIENT'S CATALOG NUMBER
4. TITLE *(and Subtitle)* Holographic Analysis of Large Vehicle Structures		5. TYPE OF REPORT & PERIOD COVERED Final, 7/80-4/82 6. PERFORMING ORG. REPORT NUMBER
7. AUTHOR(s) G.R. Gerhart G. Arutunian J.M. Graziano		8. CONTRACT OR GRANT NUMBER(s)
9. PERFORMING ORGANIZATION NAME AND ADDRESS US Army Tank-Automotive Command DRSTA-ZSA Warren, MI 48090		10. PROGRAM ELEMENT, PROJECT, TASK AREA & WORK UNIT NUMBERS
11. CONTROLLING OFFICE NAME AND ADDRESS		12. REPORT DATE July 82 13. NUMBER OF PAGES
14. MONITORING AGENCY NAME & ADDRESS*(if different from Controlling Office)*		15. SECURITY CLASS. *(of this report)* UNCLASSIFIED 15a. DECLASSIFICATION/DOWNGRADING SCHEDULE
16. DISTRIBUTION STATEMENT *(of this Report)* Approved for public release: distribution Unlimited		
17. DISTRIBUTION STATEMENT *(of the abstract entered in Block 20, if different from Report)*		
18. SUPPLEMENTARY NOTES		
19. KEY WORDS *(Continue on reverse side if necessary and identify by block number)* Holography, Lasers, Interferometry, Vibration		

20. ABSTRACT *(Continue on reverse side if necessary and identify by block number)*

A highly tuned, double pulse, Q-switched ruby laser is used to make double exposure holograms of large vibrating objects. The holographic fringe patterns are interpreted to produce a detailed knowledge of the displacement amplitude for a wide variety of vibrating objects. A triggering system permits the firing of the laser relative to arbitrary phase orientations of the vibrating object. A primary emphasis is placed upon the holograms at the same amplitude and frequency but different phase angles yields valuable information about

DD FORM 1 JAN 73 1473 EDITION OF 1 NOV 65 IS OBSOLETE

UNCLASSIFIED

SECURITY CLASSIFICATION OF THIS PAGE *(When Data Entered)*

the dynamics of the vibrating vehicle components. These interferometric fringe patterns reveal important information about global displacement amplitude and stress concentrations.

TABLE OF CONTENTS

FIGURES

1. OBJECTIVE

Double pulse holography is utilized to study the mechanical deformation properties of very large vehicle components. The holographic fringe data are analyzed in order to obtain global dynamic information over large sections of the vibrating vehicle surface. This information provides a means for improving vehicle desing and performance while reducing the level of acoustic and structural vibration.

2. INTRODUCTION

Several years ago, basic and applied research programs were initiated on holographic interferometry at TACOM. Continuous Wave (CW) holography was first utilized with a HeNe laser to investigate the acoustic and vibrational characteristics of relatively small components. The exposure times for these holograms were quite long because the photographic film speed was slow and the HeNe laser had a low power output. Since the exposure time intervals were several seconds in duration, the very low frequency building and environmental background vibration levels caused considerable problems unless the test components were put on an isolation table. This latter requirement puts severe limitations on the size and location of the holographic test specimens.

The CW holographic interferograms consisted of time average, double-exposure, and real time holograms. The quality and reproducibility of these holograms were excellent. The real time holograms were quite useful because a single exposure can be used to view the fringe pattern over a wide range of vibration frequencies. An acoustical-optical modulator was used to gate the CW laser beam and provide excellent real time fringe contrast. The time average interferograms produced excellent quality fringe patterns which were limited to a single vibration frequency.

Continuous wave (CW) holographic techniques, which utilize HeNe or argon laser light sources, are limited in a number of ways. The test object in CW holography has to be isolated from the environment because the maximum tolerable motion of the experimental apparatus is about one-eighth of the laser light wavelength. CW holographic interferometric techniques are restricted to the measurement of very small amplitudes. A maximum displacement amplitude of about 25 wavelengths is possible using strobe light techniques such as acoustical-optical modulators.

These limitations with CW holography can be circumvented by using double pulse holographic techniques. This work is based on our results which are obtained with a holographic camera that employs a Q-switched ruby laser. Each laser pulse has a duration of approximately 30 nano-seconds which is much less than the periods of the vibrating structures. The separation time between pulses varies from a few microseconds up to about one millisecond while typical values usually range between 200 and 500 microseconds. Pulse separation time intervals are kept less than one millisecond to avoid isolation problems with the low frequency building vibrations but are still long enough to record surface displacement occurring at the frequencies of interest. These pulse separation times are much shorter than the vibration periods of large amplitude displacement functions in order to maintain observable fringe densities.

Double-pulse holography also provides a measurement technique for the analysis of vibrating components with large surface areas. A particular advantage of pulse holography is that ruby lasers can be designed to provide a very large output energy for the uniform illumination of large mechanical structures. Holography in general requires no contact with the test specimen, and it gives a solution to a classical problem in the areas of both acoustic and vibration analysis. The surface motion is represented by a fringe pattern which connects points that have the same displacement during the time interval between the two pulses. Since holography is based in interferometry, the accuracy of the object motion is measured to within a fraction of the wavelength of light.

3. DESCRIPTION OF EQUIPMENT

A Korad model K1400QDH/KHCL holographic camera was used to produce the holograms. This camera consists of three units: the camera head, Figure 3.1, two power supplies, Figure 3.2, and a closed cycle water cooling system. The laser head is mounted on a heavy duty camera tripod, which can be swiveled and angled to permit the illumination of objects with complex geometries. All the units are mounted on wheels and are reasonbly portable. The complete system is shown in Figure 3.3. A diagram of the optical layout of the laser head is shown in Figure 3.4. Low energy laser radiation is generated by the ruby oscillator cavity (bottom of figure) and transmitted through two ruby crystal amplifiers. The resulting amplified radiation is divided into two equal intensity divergent output beams. A part of the amplified laser beam within the optical head is split off and used for a reference beam and beam energy monitor. The interference pattern resulting from the interaction of the light reflected from the vibrating object and reference beam is recorded on film that is located on top of the front end of the laser head. The most critical part of the holographic system is the ruby oscillator cavity, Figure 3.5, that consists of rear and front etalons, Pockels cell Q-switch and the ruby rod. The two etalons contain Fabry-Perot elements that are individually tuned by controlling the temperature to within $0.2^{o}C$. This is accomplished by using insulated enclosures and resistive heating elements with appropriate control circuits to maintain a very uniform etalon temperature over long time intervals. In addition, by incorporating extra reflecting elements in the rear etalon, the temporal coherence is increased by decreasing the TEM_{oo} line width.

The temporal coherence length of each holographic exposure can be monitored by using a Fabry-Perot (FP) interferometer mounted on a bracket along side of the holographic camera head. The FP interferometer, Figure 3.6 consists of a Fabry-Perot etalon, a diverging lens, and a Galilean telescope with a magnification of 15.A Polaroid camera back records the interference pattern that consists of concentric circular rings of various diffraction orders. The laser

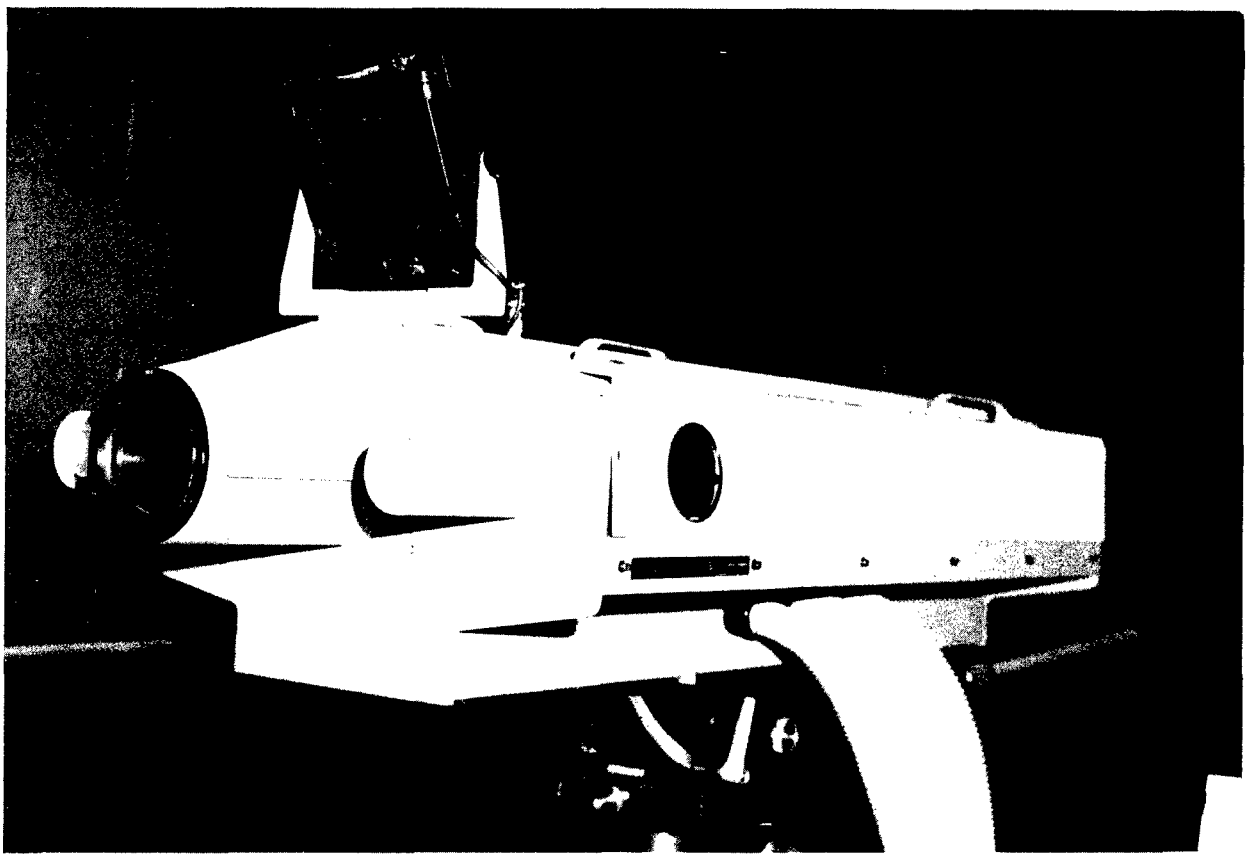

Figure 3.1

Holographic Camera Head. The Film Holder is located on Top and Front of the Output End.

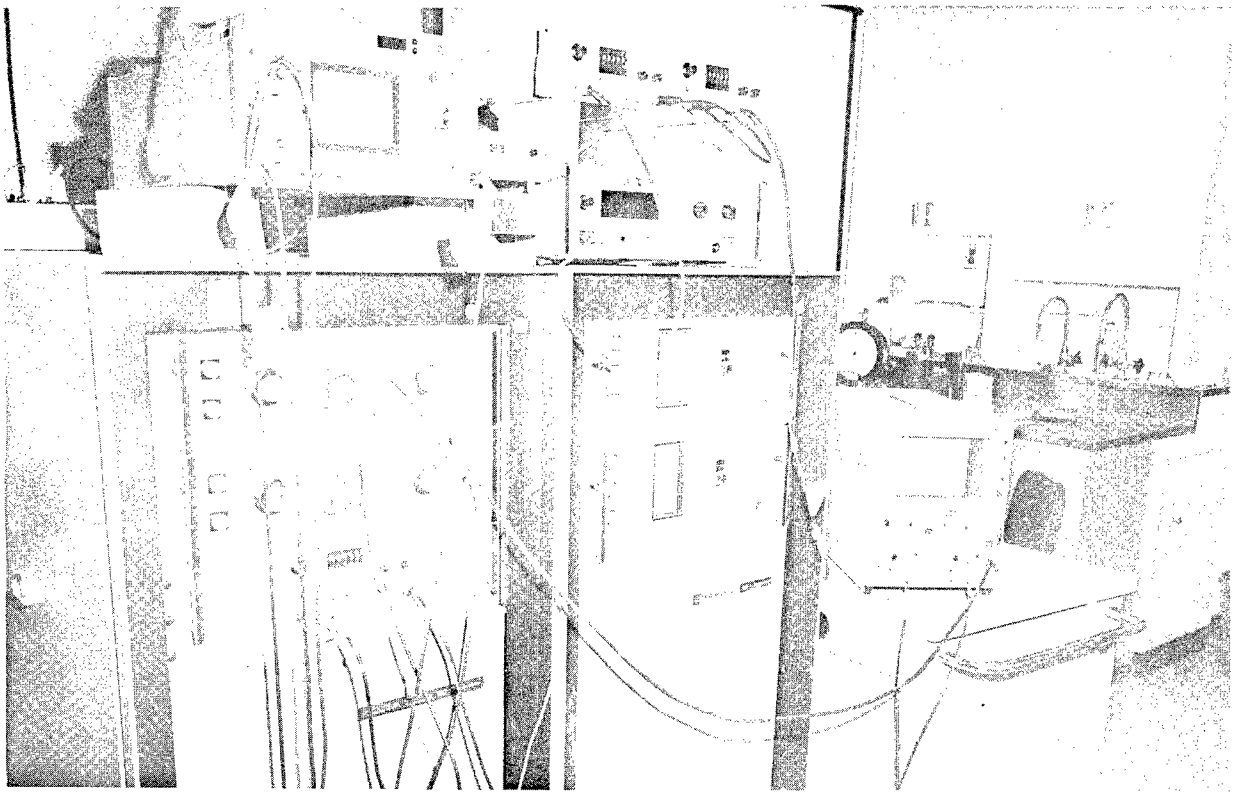

Figure 3.2

Laser Power Supply and Firing Controls with Ancilliary Monitoring Instrumentation

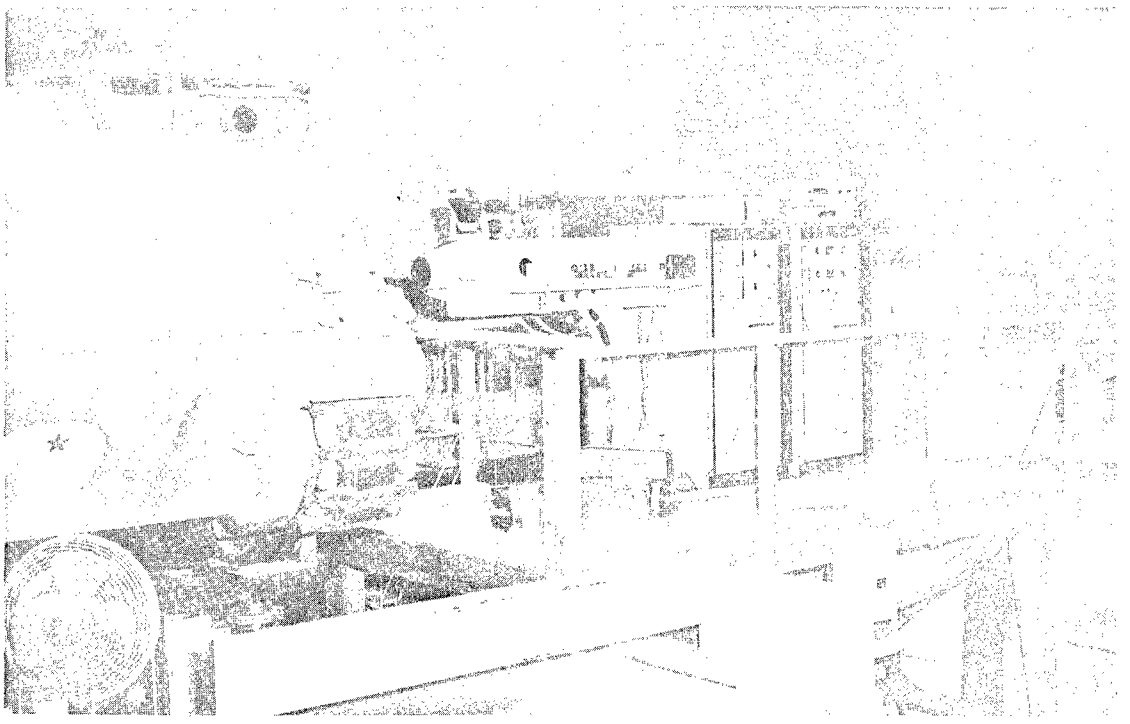

Figure 3.3

The Holographic Camera Facing Test Vehicle

OPTICAL LAYOUT FOR REFLECTION HOLOGRAPHY

Figure 3.4

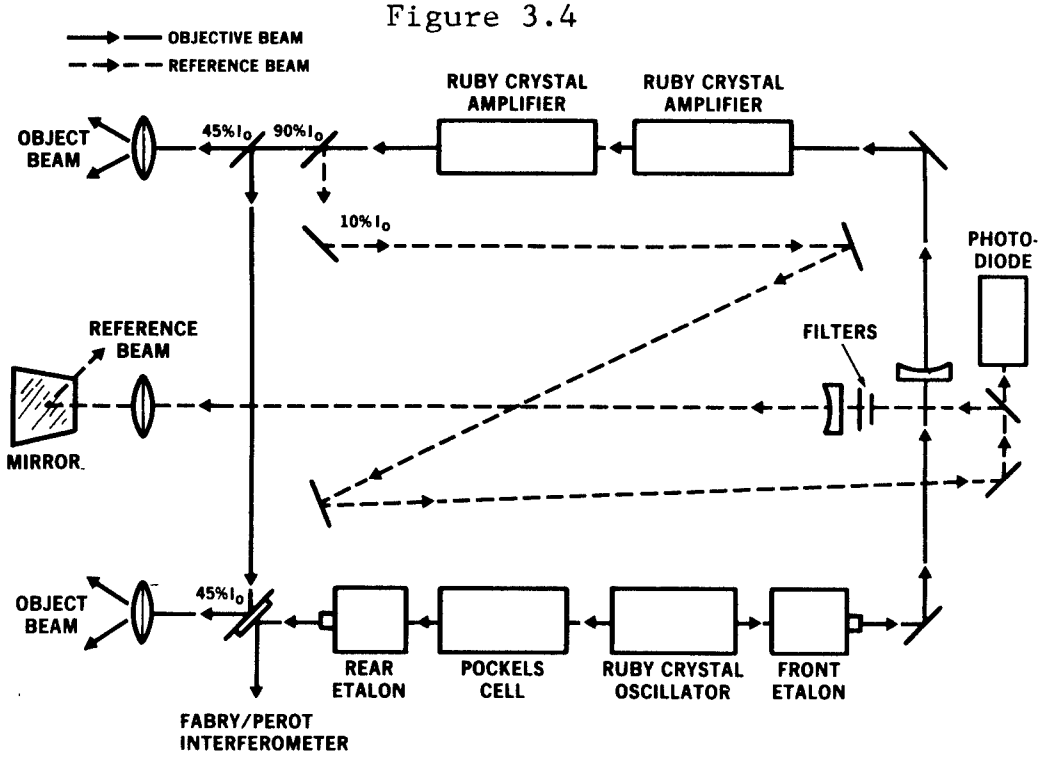

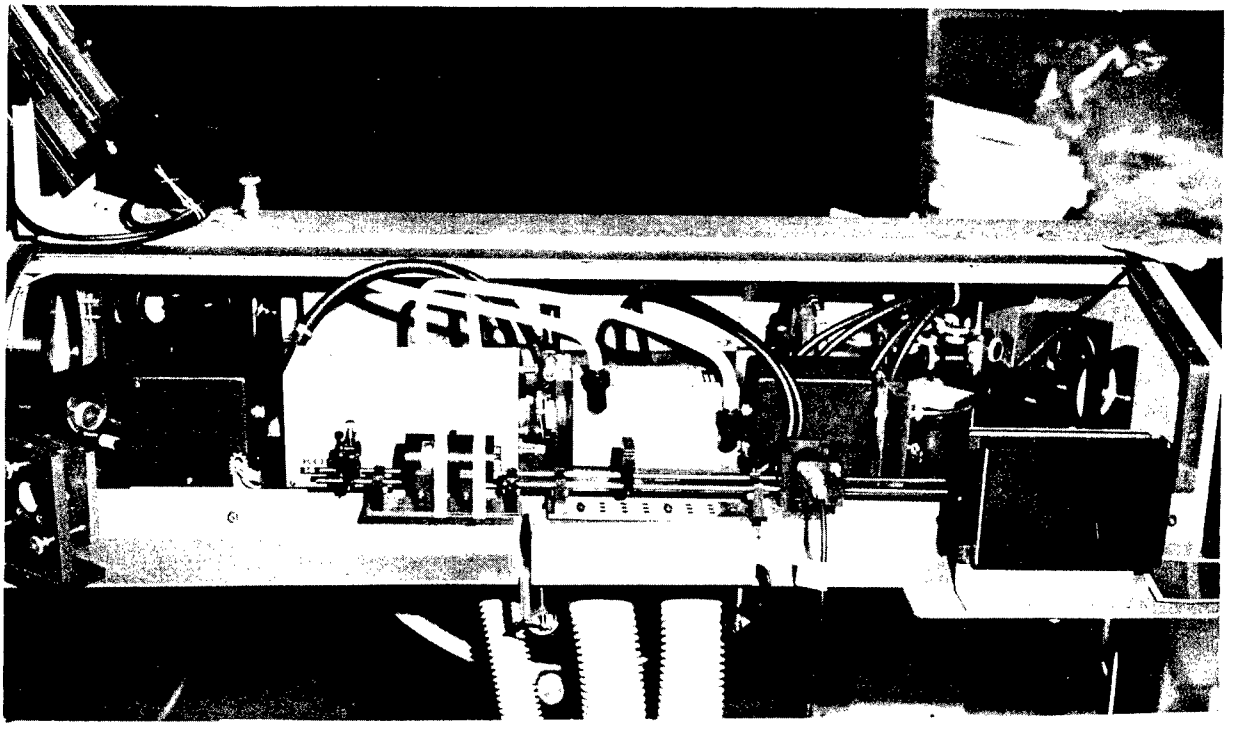

Figure 3.5

Side View of Laser Oscillator Cavity. In this Photograph the following Elements are Visible From Left to Right: Rear Etalon, Pockels Cell, Ruby Oscillator Housing, and Output Etalon.

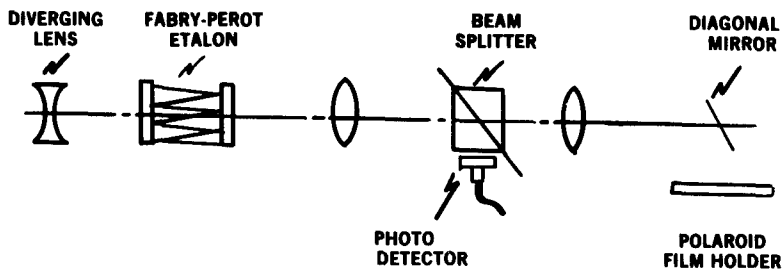

Figure 3.6

Diagram of the Fabry-Perot Interferometer for Determing Laser Mode Content.

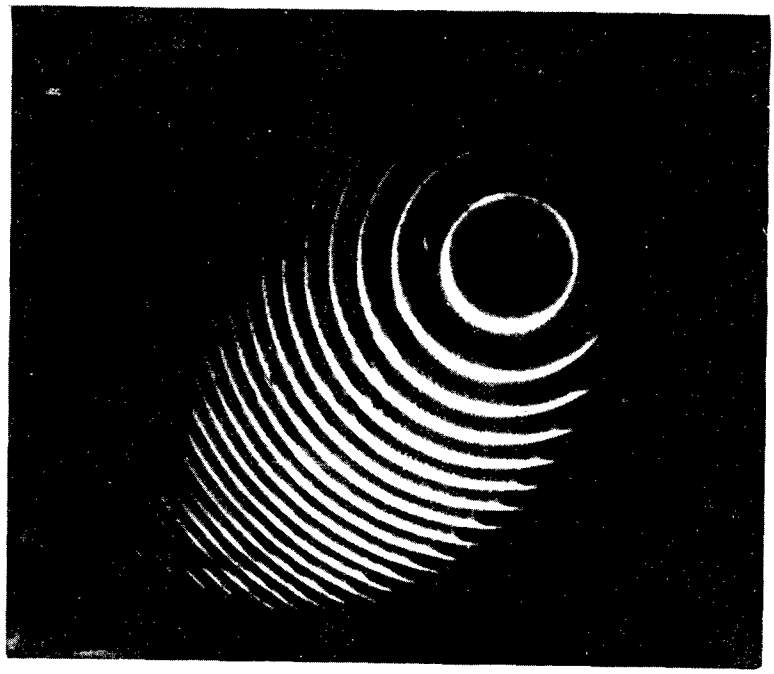

Figure 3.7

Single Model Interference Pattern of Ruby Laser Output. This Example Represents a Coherence Length of 7 Meters.

output is multi-moded if these interference orders have a multiple structure. Figure 3.7 is an example of an interference pattern for a double pulse, single mode laser output. Each of the diffraction orders is a singlet and the relative temporal coherence of the two pulses is greater than 7 meters. Figure 3.8 is a FP interference pattern where the output energy is distributed over several longitudinal cavity modes. The relative temporal coherence of this double pulse output is only a few centimeters.

For maximum temporal coherence stability, the laser oscillator is tuned to emit light just above a threshold energy of 5 millijoules per pulse. The laser output is Q-switched to produce a pulse width of 20 to 30 nanoseconds which after two stages of amplification is increased to a peak power output of 100 megawatts or an average of 2 joules per pulse.

Consistent single-mode, double-pulse laser output requires a temperature control of the oscillator ruby rod to within $0.1^{o}C$ to maintain longitudinal mode stability. In addition, the room temperature must be held nearly constant to within a narrow range of a few degrees centigrade in order to maintain steady state heat transfer in the aluminum base plate and optical and electrical components. Once these conditions are achieved only a minimum amount of skill and tuning are required to obtain consistent single mode double pulse exposures.

A time history of the vibration patterns relative to the instantaneous object motion is important for large complex vibrating structures such as automotive and military vehicle components. The "fire" button in the original design of the holo-camera initiates an internally generated electronic sequence which opens the film shutter approximately 0.2 sec before firing the laser flashlamps. This procedure produces a delayed holographic exposure that is not synchronized relative to the vibrating object. Holograms obtained in this manner have a random time orientation relative to the periodic motion of the vibrating object.

To extend and improve the capability of our holographic technique, two modifications were made that permitted exposures in sequence relative to some reference signal. First, the shutter was disconnected from the laser firing circuit and manually triggered, which eliminated the built-in 0.2 second delay. Second, the internal triggering circuit was modified by disconnecting the time delay circuits and firing the laser flash-lamps directly by means of an external solid state switch, which reduced the trigger delay time to a consistent 75 microseconds. The external solid state switch was switched "on" by gate pulse from a 2 channel-storage oscilloscope inserted in the laser firing circuit as shown in the upper part of Figure 3.9.

A typical sequence of electronic events can be described as follows: the manual single shot trigger on the storage oscilloscope initiates a beam sweep across the CRT for a preset amplitude and slope level of the trigger waveform. A 5 volt gate pulse is simultaneously generated which triggers

Figure 3.8

Multi-Mode Ruby Laser Output

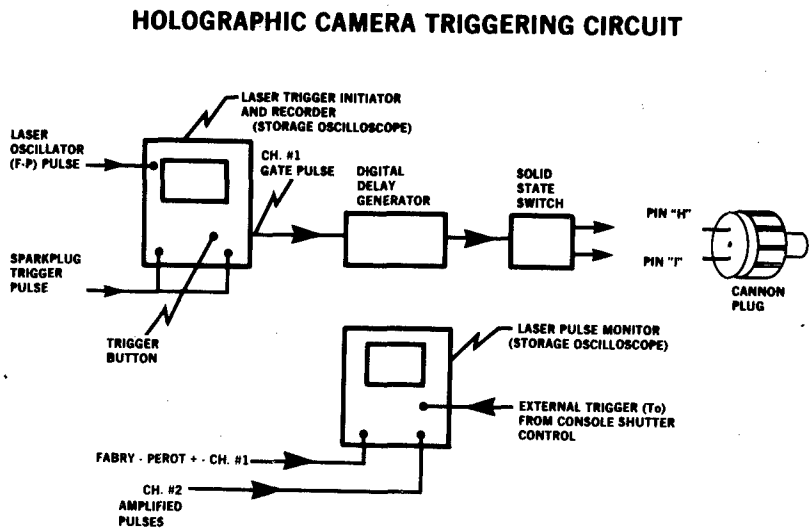

Figure 3.9

Modified Holographic Camera Triggering Circuit.

a digital delay generator. The delayed output initiates the solid state circuit which ultimately fires the laser. The relative phase between the exciting wave form or trigger source and laser output is easily varied by adjusting the digital delay.

Typical storage oscilloscope traces of the laser pulses and the reference trigger pulse are shown in Figure 3.10. The double laser pulse (top trace) with a 150 microsecond pulse separation time, and the triggering waveform (bottom trace) are displayed simultaneously on the 2-channel storage oscilloscope. The reference trigger pulse is obtained by wrapping a single turn of copper wire around the No. 1 spark plug cable of a 4 cylinder-4 cycle M151 $\frac{1}{4}$-ton truck engine as shown in Figure 3.11. A 5 megohm resistor in series with the inductive pick up was required to reduce the voltage level to the operating range for the oscilloscope input. In Figure 3.10, the engine is running at 3,000 RPM with the laser firing 5 msec after the No. 1 spark plug pulse. The sweep rate of the oscilloscope is adjusted so that the two trigger pulses are displayed during a time interval of 2 engine revolutions or 720^{o} of rotation.

External excitation of the vehicle body was done with a piezoelectric-magnetostrictive vibration generator system which was bolted on the cowl of the vehicle as shown in Figure 3.12. An example of double pulse laser illumination of the vehicle at 66 Hz is shown in Figure 3.13. At higher excitation frequencies, however, the second illumination pulse will occur several periods after the first as shown in Figure 3.14 for a 16.3 KHz excitation of a turbine blade. An electronic block diagram of the vehicle shaker system is shown in Figure 3.15. The magnitude of the force imparted to the vehicle was varied by an attenuator inserted in the oscillator output. A piezoelectric force and accelerometer transducer gage attached to the vibration generator head monitored the force and acceleration level at the point of attachment on the vehicle.

4. RECONSTRUCTION AND PHOTOGRAPHY

A HeNe continuous wave (CW) laser was used to reconstruct the holograms in this report. A 35mm camera using Kodak 2615 red sensitive film was particularly effective for photographing the virtual image of the pulse holograms. These holograms were recorded on 4 in x 5 in Agfa-Gaevert film and plates which were developed in D-19 solution for approximately 3-5 minutes. Since the reconstruction beam was not identical in curvature to the original reference beam, a corrective lens was placed in the reconstruction beam to compensate for these effects. The result was a much clearer image over a wider field of view.

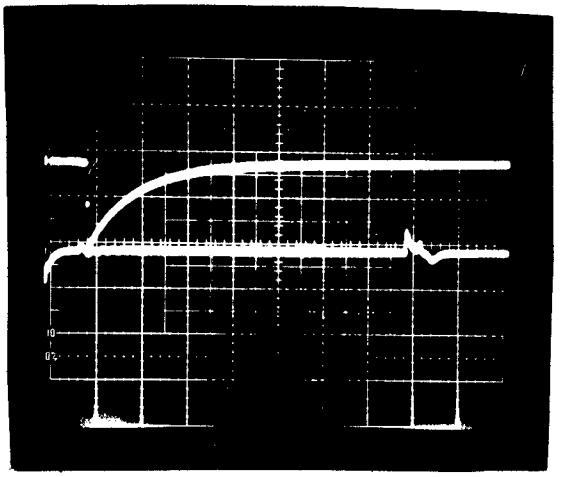

Figure 3.10

Double Pulse Laser Illumination (Top Trace); Spark Plug Trigger Output (Bottom Trace) with Engine Running at 3000 RPM. Distance Between the Beginning of the Bottom Trace and Pulse Represents 2 Engine Revolutions.

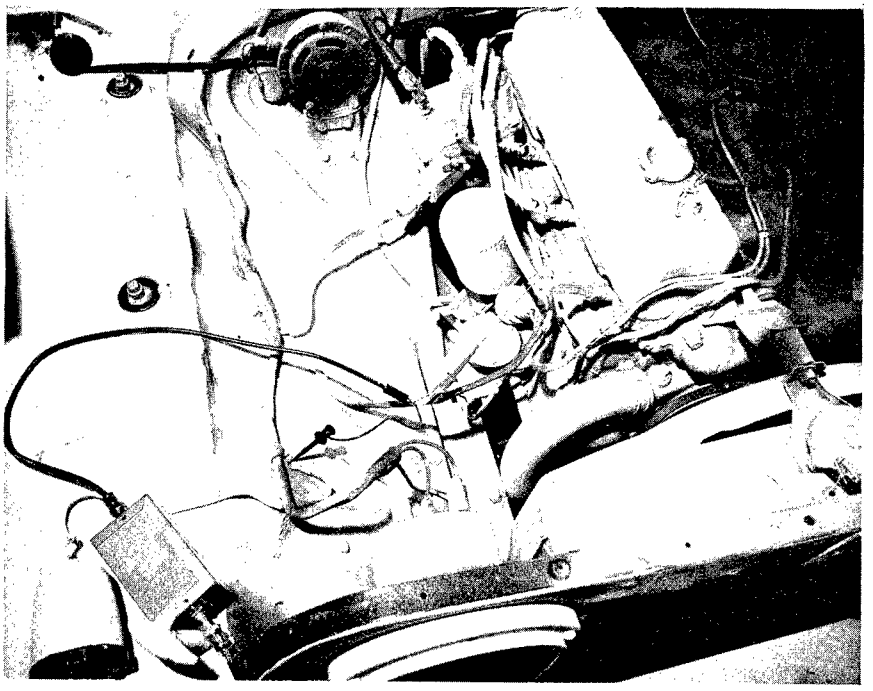

Figure 3.11

Top View from the Front End of the M151 Engine Spark Plug Trigger Connection.

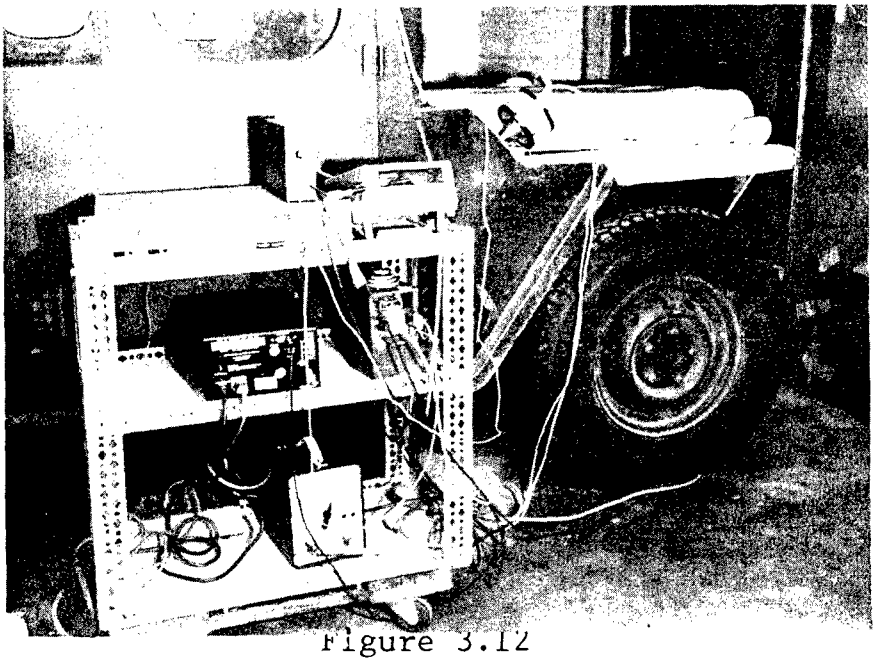

Figure 3.12

Electro-Magnetic Vibrator Instrumentation with the Vibrator Head Attached to Vehicle.

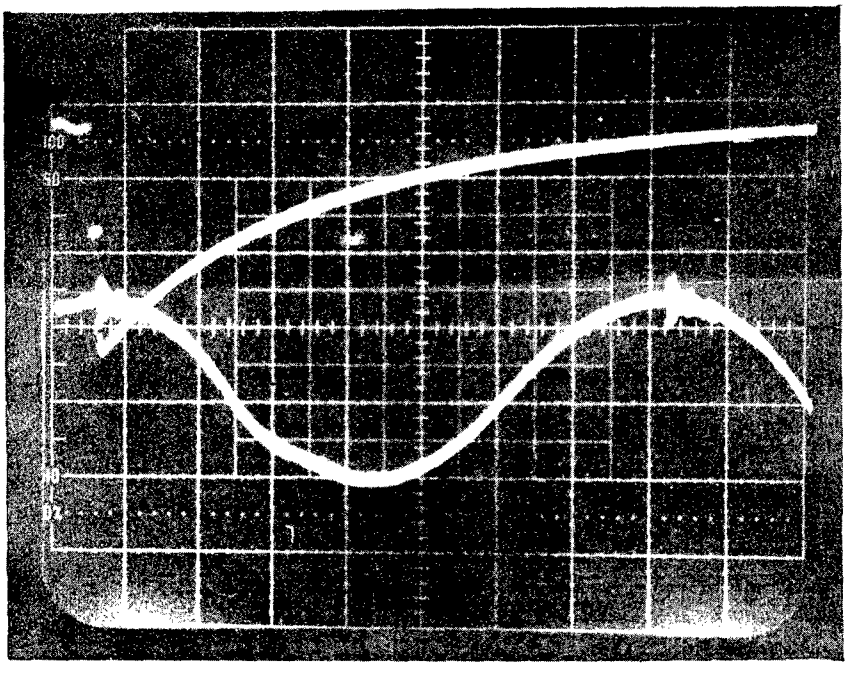

Figure 3.13

Illumination (Top Trace) of a Vehicle Being Shaken at a Frequency of 66 Hz (Bottom Trace). The Laser Pulse Separation is 150 Microseconds. Laser Illumination is Occurring at the Peak of the Sine Wave.

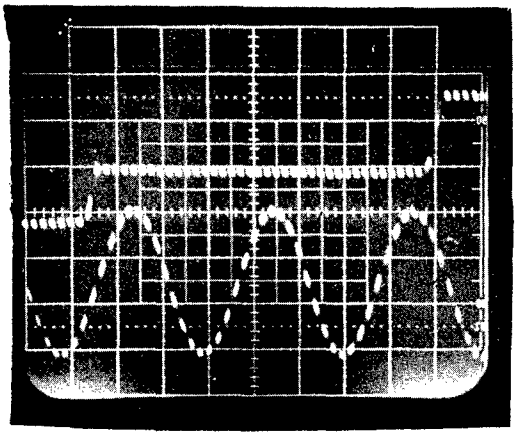

Figure 3.14

Double Pulse Illumination of a Turbine Blade at 16300 Hz. The First Pulse is Triggered Slightly Before the Sinewave Peak while the Second Pulse is Fired 150 Microseconds Later During the Third Cycle. The Dashed Lines are Due to the Resolution of the Chopping Frequency by the High Sweep Rate.

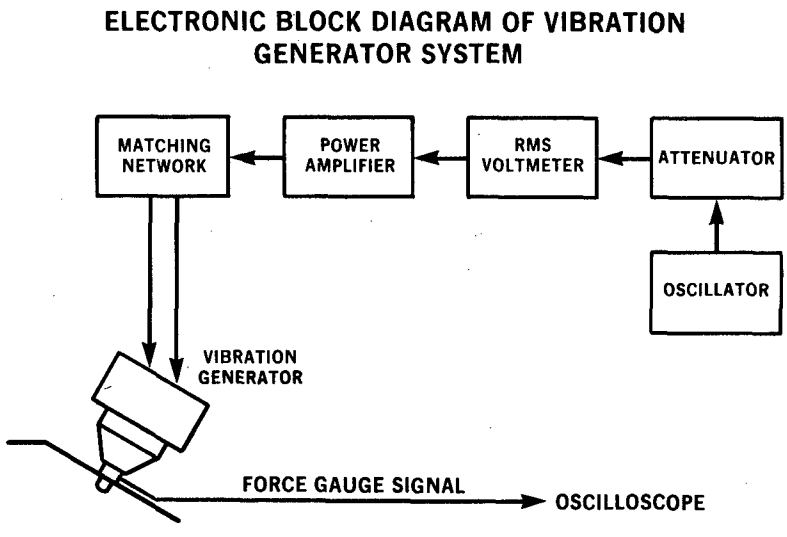

Figure 3.15

Electronic Block Diagram of the Wilcoxon Vibration System

5. DISCUSSION OF RESULTS

An example of 7 meter coherence length holography is shown in Figure 5.1 which is a hologram of a 3.5 meter test board with black vertical lines 20 cm apart. It should be mentioned that only 75% of the board is visible in this photograph, however, the entire board and the back wall of the room are visible when viewing the holographic image with the naked eye. Figure 5.2 is a double pulse hologram of a vacuum pump drive with an electric motor running at 1,725 RPM. The parallel fringes on the exhaust baffle and intake tube are caused by rotational cantilever motion while the "bull's eye" pattern on the base and side panels are due to complex mode excitations. A double pulse hologram of a man, Figure 5.3 standing 2 meters in front of the camera reveals the tiny muscle movements of the human body as indicated by the fringe contours on the laboratory coat. The regions of highest fringe density have the largest amplitudes of vibration. The fringe contrast in this hologram is high because the two ruby pulses have nearly identical amplitudes. The pulse separation time between the two laser pulses is about 500 microseconds. Although designed for large structure holography, the capability of this camera for illuminating small objects is shown in Figure 5.4 where a solid turbine compressor blade excited at a frequency of 16.3 KHz.

The first military vehicle which was selected for holographic analysis was a M151 $\frac{1}{4}$-ton utility truck. This vehicle is shown in Figure 5.5 with an artic cab kit. A water soluble white paint was applied to the vehicle to increase the reflectance of the surface. The driver's side of the vehicle was struck with a plastic tipped hammer to produce an impulse force. The vehicle continued to vibrate for a period of time after the impact before damping to zero. The ruby laser was fired manually a short time after the impact as shown in Figure 5.6. Several other holograms were also taken in the same manner with a random time interval between the laser pulses and the hammer impact. The resulting fringe patterns differed significantly in fringe spacing and contour. This assortment of holographic fringe patterns is useful for studying the entire motion of the vehicle surface during one cycle of the periodic displacement. A more systematic approach would utilize an external triggering circuit to vary the time interval between impact and the laser pulses by a constant value. The latter technique provides a more reproducible method for obtaining a time sequence of double exposure holograms. Figure 5.7 is an identical configuration to Figure 5.6 except that the time interval between impact and the laser firing is much longer for the latter. The fringe spacing in Figure 5.7 is much larger because the vibration amplitude is considerably more attenuated when compared with Figure 5.7.

The largest fringe densities in Figures 5.6 and 5.7 are clearly located on the door panels. These panels consist of thin sheet metal which is fastened with screws over the door frame. The regions with complex circular fringe patterns are relatively isolated from one another by the interior structure of the door. The fringe lines are regions of constant differential

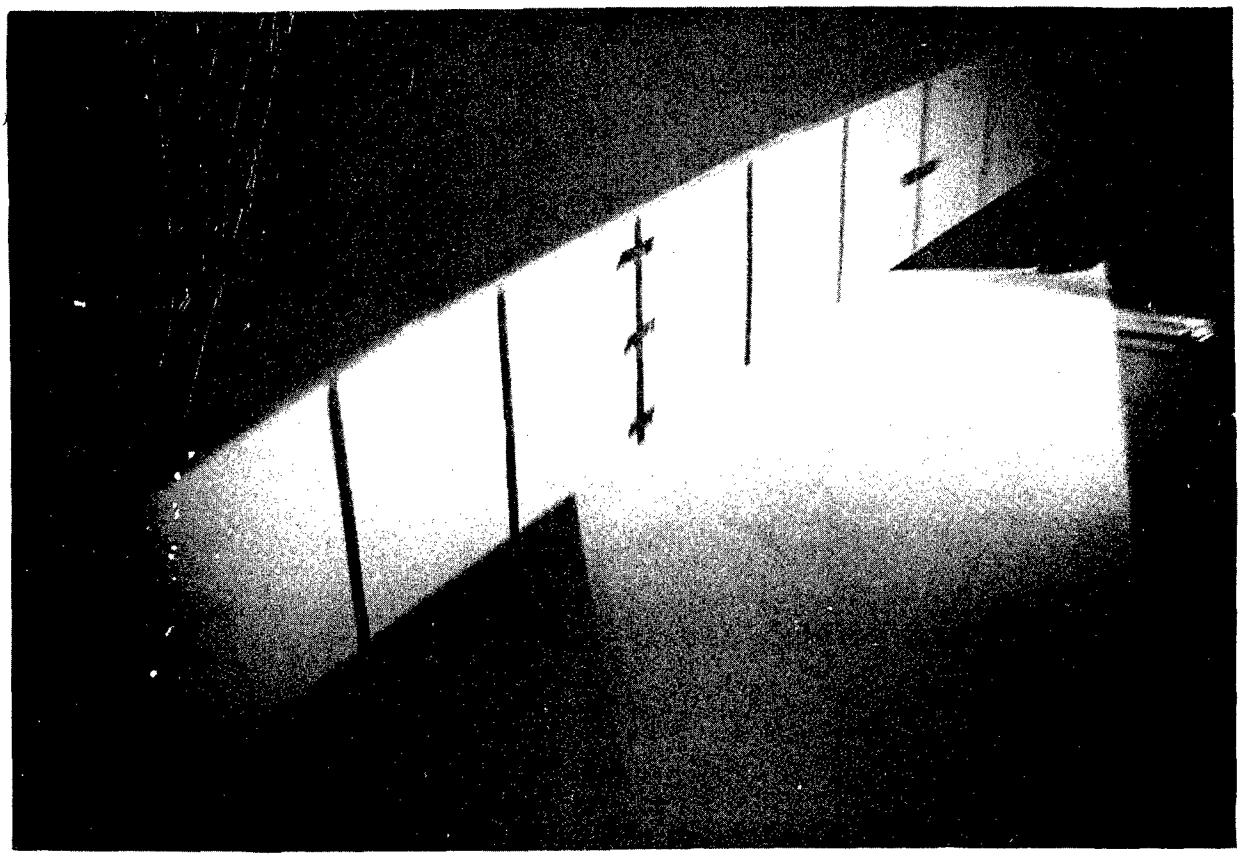

Figure 5.1

Hologram of 3.5 Meter Board Illustrating 7 Meter Coherence Length. Vertical Lines are 8 Inches Apart.

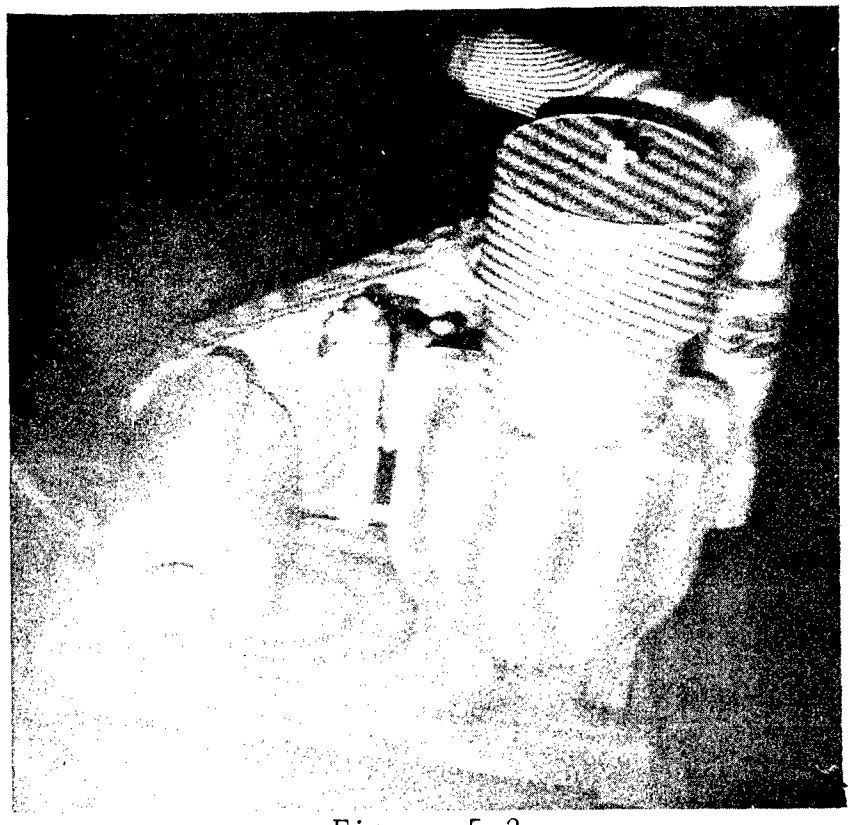

Figure 5.2

Fringe Pattern Generated on a Vacuum Pump Driven by an Electric Motor.

Figure 5.3

Hologram of a Man Showing the Minute Vibration Patterns Transmitted to Outer Clothing by Natural Body Movements.

Figure 5.4

An Example of a Small Area Double Pulse Holography of a Turbine Compressor Blade Excited at 16300 Hz. Pulse Separation 150 Microseconds.

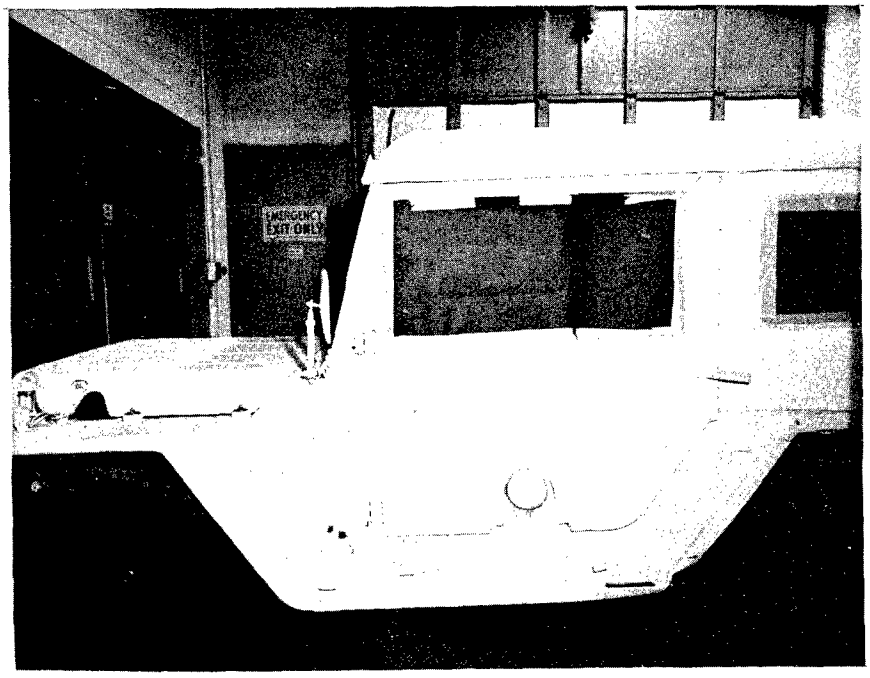

Figure 5.5

Position of Vehicle for Sideview Holography. Driver's side of Vehicle is Painted White to Enhance Light Reflectivity.

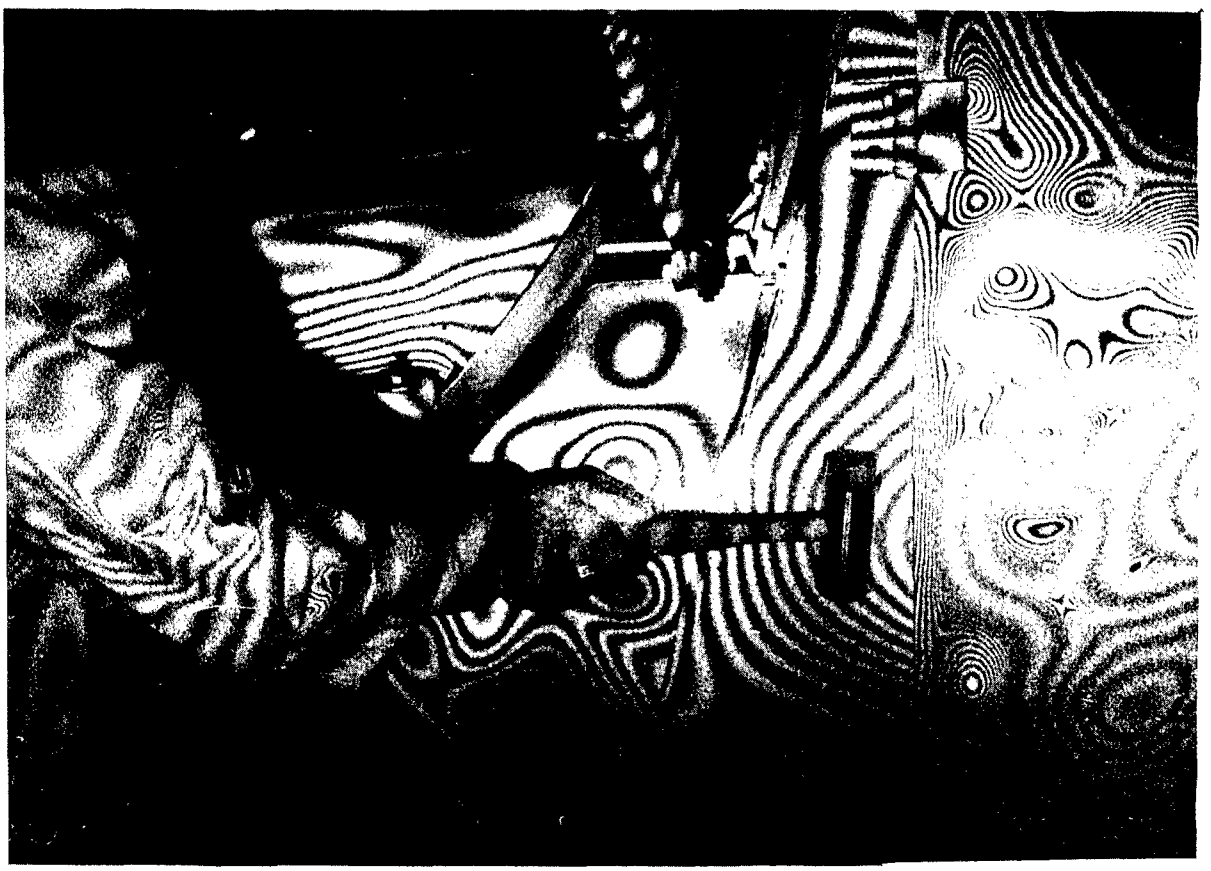

Figure 5.6

Hammer Impact on the Side of the Vehicle which is Characterized by the Development of Complex Fringe Patterns on the Thin Sheet Metal. Laser Pulse Separation Δt=150 Microseconds.

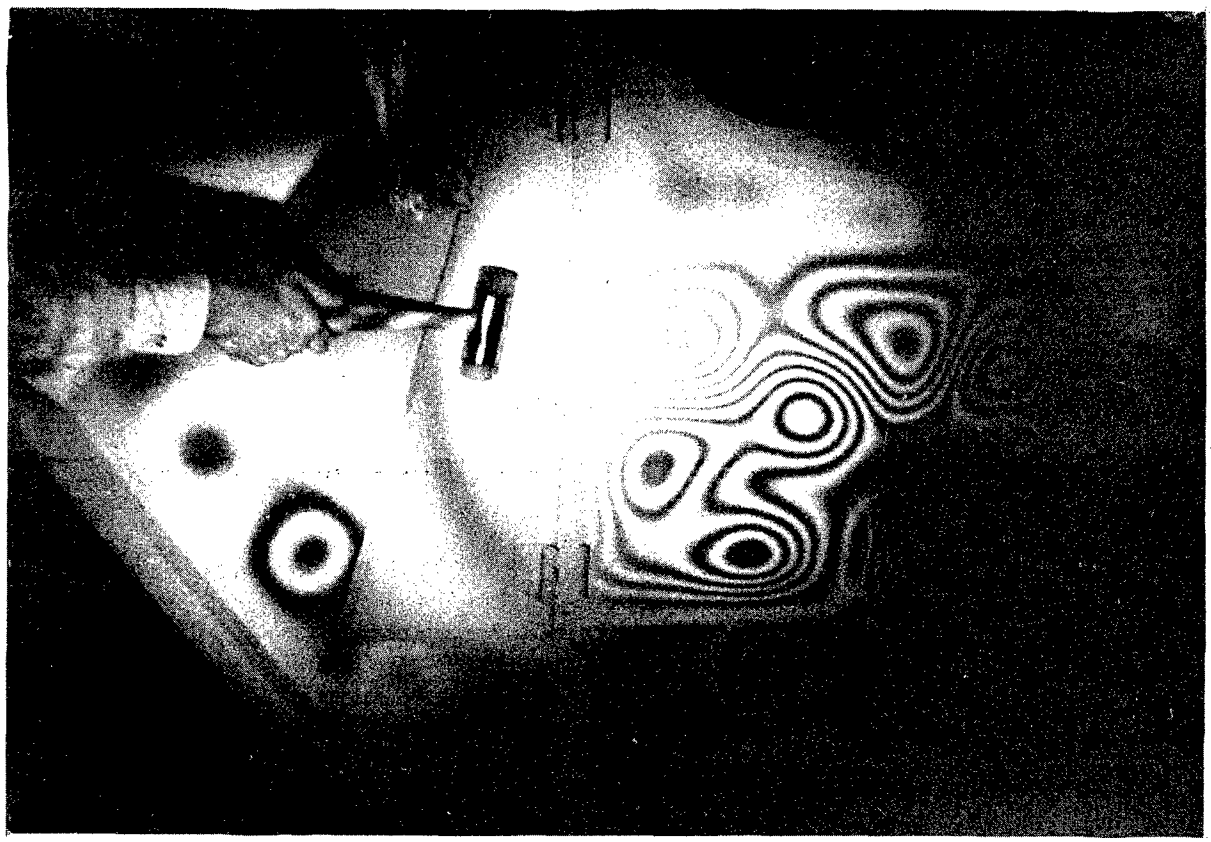

Figure 5.7

Hammer Impact. Damping at Point of Impact Indicates Late Laser Illumination. Δt=150 Microseconds.

displacement or constant average velocity during a time interval Δt. Regions which have large fringe densities correspond to large surface velocity variations. These areas are particularly important in acoustic power radiation determinations.

Figure 5.8 is a double exposure hologram of the rear portion of the left door panel. A hammer blow is ~~also~~ exciting the structure at a point between a pair of "bull's eye" fringe patterns. Note that these circular fringe patterns are nearly identical, except for fringe contrast reversal.

An ideal situation would be to obtain holographic exposures of a military vehicle while it is actually traversing over typical terrain conditions. This procedure would provide a real-time evaluation of the complex interaction of the road and engine induced vibration on vehicle components. The rigid body motion of the vehicle, however, would generate a large number of fringes which would obscure the deformational motion of the vehicle. A more feasible approach might be to simulate off-road conditions by using a large hydraulic shaker to which the vehicle is mounted on four independent actuators. Each actuator would be driven by a forcing function derived from field data. A more practical approach for our limited resources was to mount a small electro-mechanical shaker on the vehicle structure and apply sinusoidal force inputs up to 50 lbs. RMS.

Figure 5.9 illustrates the test configuration of the M151 from a frontal view of the vehicle. The force transducer is bolted to the front cowl in the left hand portion of the photograph. The vehicle is excited at a structural resonant frequency of 66 Hz at two force levels of 27 lb and 50 lb. Double pulse holograms of the M151 at these two force inputs are shown in Figures 5.10 and 5.11. The relative phase orientation of the laser pulses and the accelerometer signal from the transducer is shown in Figure 3.13 and it is roughly the same for both holograms. The regions near the head light assemblies and the radiator grill have comparatively large fringe densities relative to the hood and cowl assemblies.

An important area of study was engine induced vibration on the body structure and engine components. This phenomenon is particularly related to the acoustic noise which is radiated from the various panels and components on the vehicle surface. Holography provides an important tool for studying the instantaneous acoustic and vibration displacement functions over large regions on the vehicle surface. This global picture is, in many instances, quite difficult to obtain using discrete transducer measurements at several locations over an extended time interval. Three examples of double pulse holograms are shown in Figures 5.12, 5.13, and 5.14 for the M151 engine operating at 1,500 and 3,500 RPM. The fringe patterns are quite dense and complex on the driver's door. The thin sheet metal structure of the door can be easiiy excited to generate large mechanical displacement. These regions are particularly efficient for generating copious amount of readiated acoustical power.

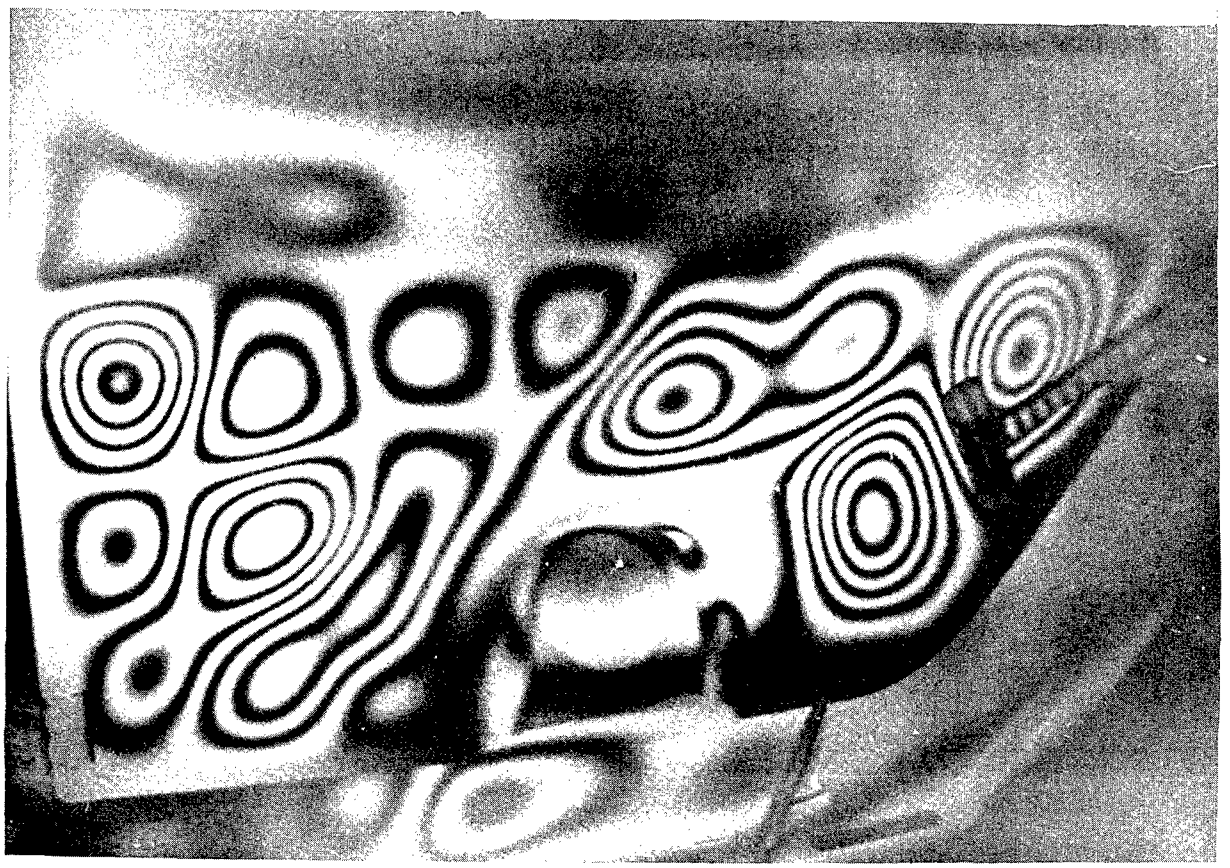

Figure 5.8

Hammer Blow on Door Showing Unusual Double Bull's Eye Pattern 180° Out of Phase. Δt=150 Microseconds.

Figure 5.9

Front End of M151 Vehicle. The Electro-Mechanical Vibrator is Mounted Behind the Right Front Fender, and Activated Remotely Prior to Laser Firing.

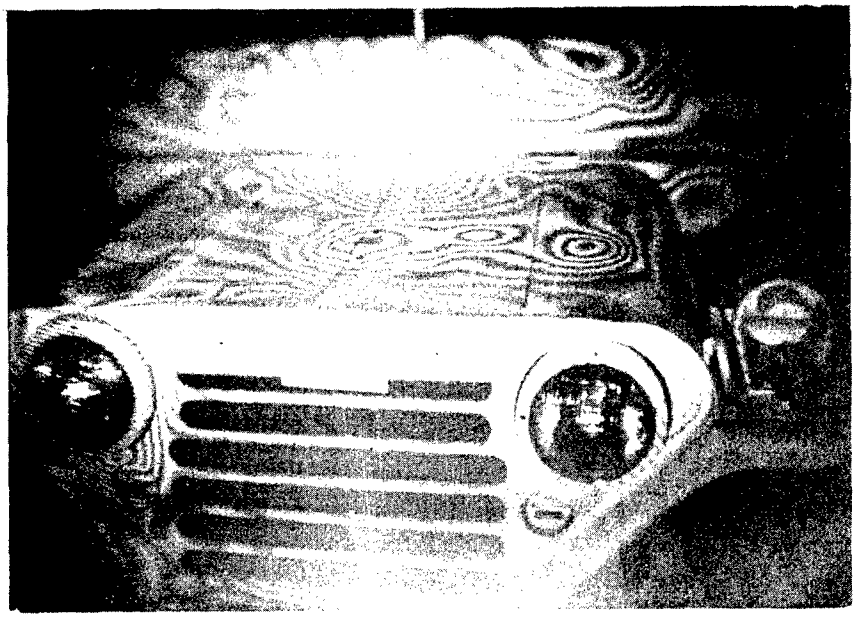

Figure 5.10

Vehicle Shaken with a 27 Pound Force at 66 Hz. Laser Pulse Separation Δt=300 Microseconds. The Thin Sheet Metal of the Hood, Windshield Frame, Front, Displays a Complex Vibrational Pattern.

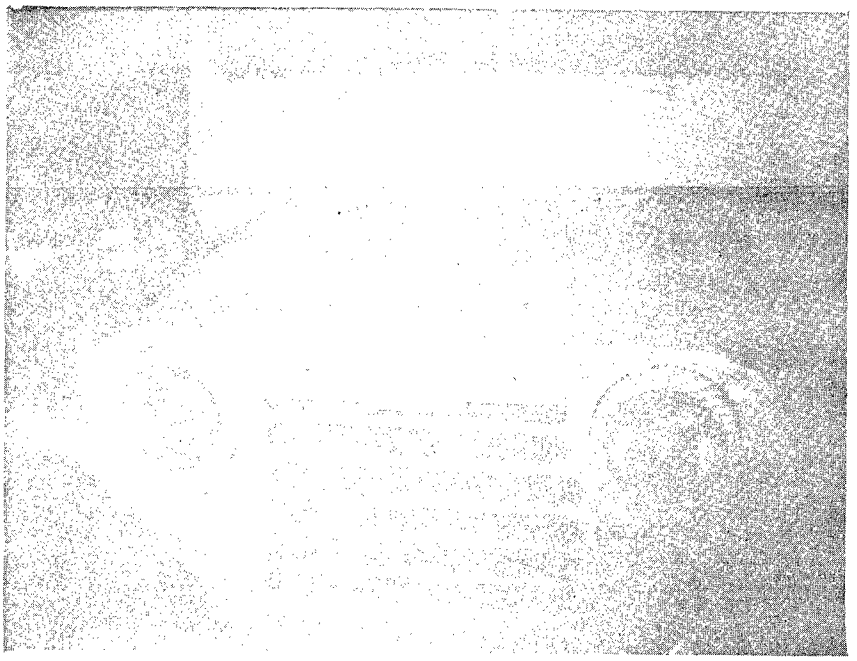

Figure 5.11

Vehicle Shaken with a 50 Pound Force at 66 Hz. The Fine Fringe Pattern Indicates a Large Vibration Amplitude. Laser Pulse Separation Δt=300 Microseconds.

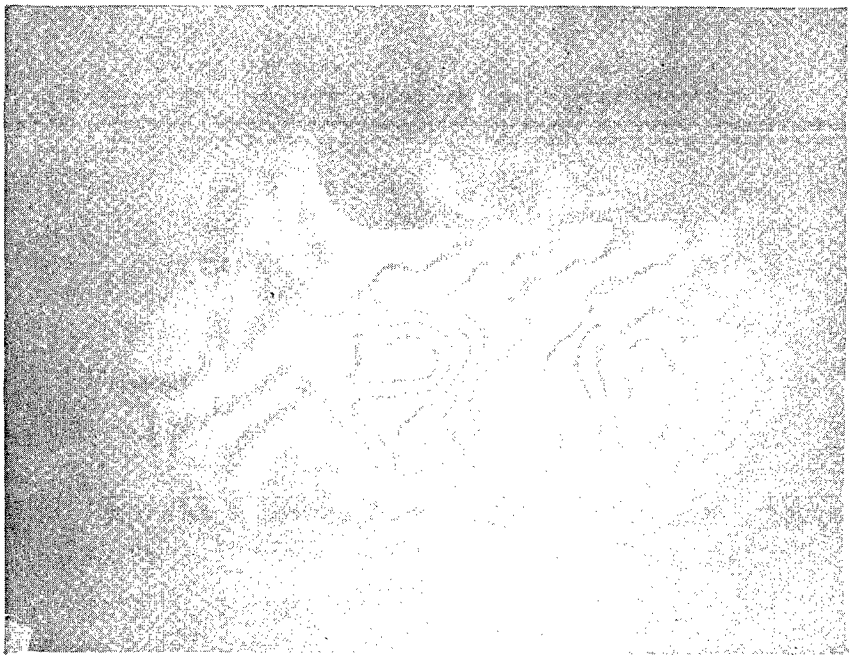

Figure 5.12

Vibration Pattern on Driver's Door with Engine Running at 1500 RPM. Random Laser Triggering with Pulse Separation Δt=300 Microseconds.

Figure 5.13

Vibration Pattern on Driver's Door at 3000 RPM. Fine Structure Indicates a Large Amplitude. Random Laser Triggering with Laser Pulse Separation Δt=300 Microseconds.

Figure 5.14

Fringe Pattern on Door Due to Accelerating Engine. Random Laser Triggering with Pulse Separation Δt=300 Microseconds.

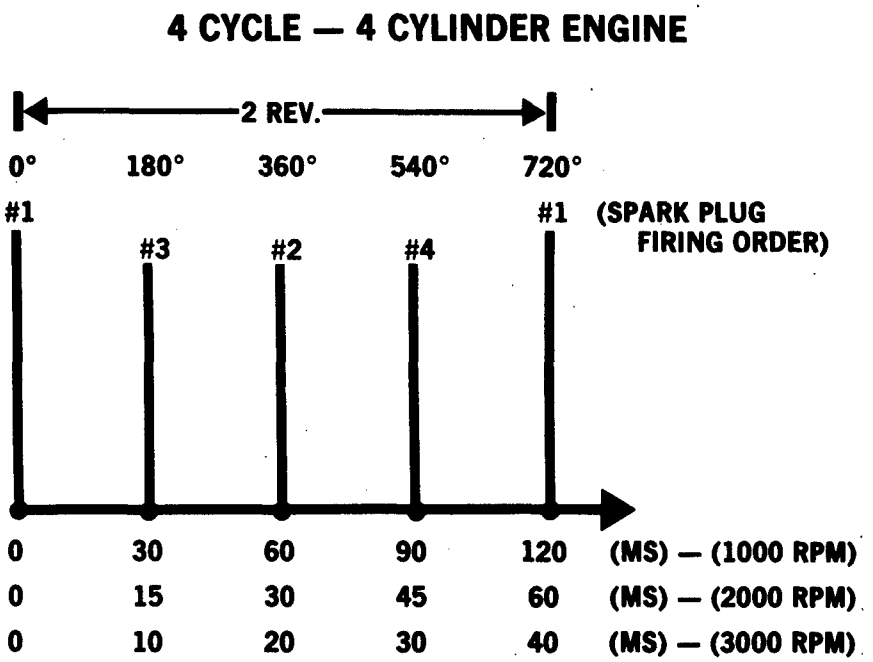

Figure 5.15

The Spark Plug Firing Sequence of a 4 Cylinder - 4 Cycle Gasoline Engine. For all Engine Holograms, the Laser Pulses were Triggered with Respect to the Firing of the #1 Spark Plug.

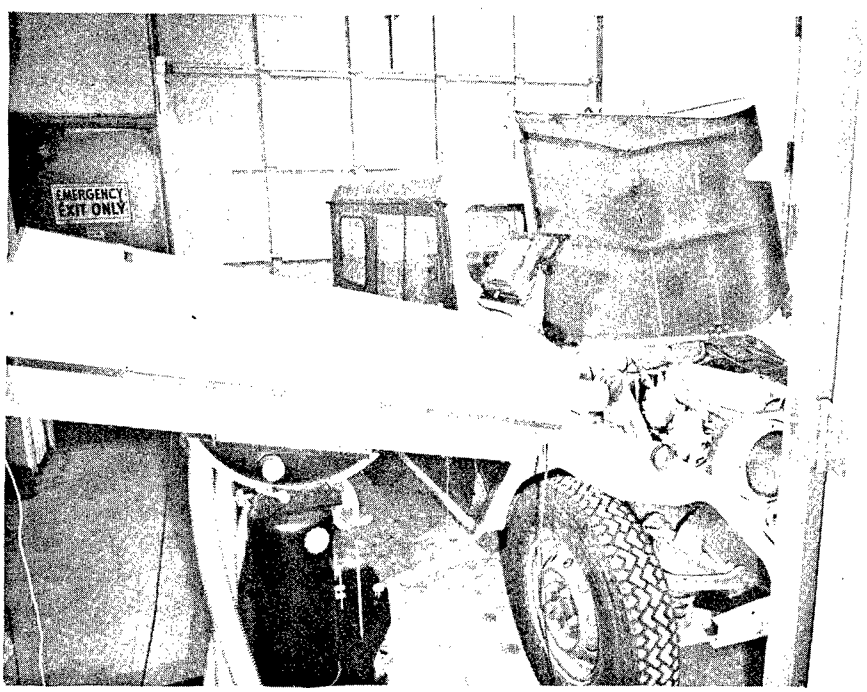

Figure 5.16

Laser Head Pointed at the Engine for Engine Holographic Exposures.

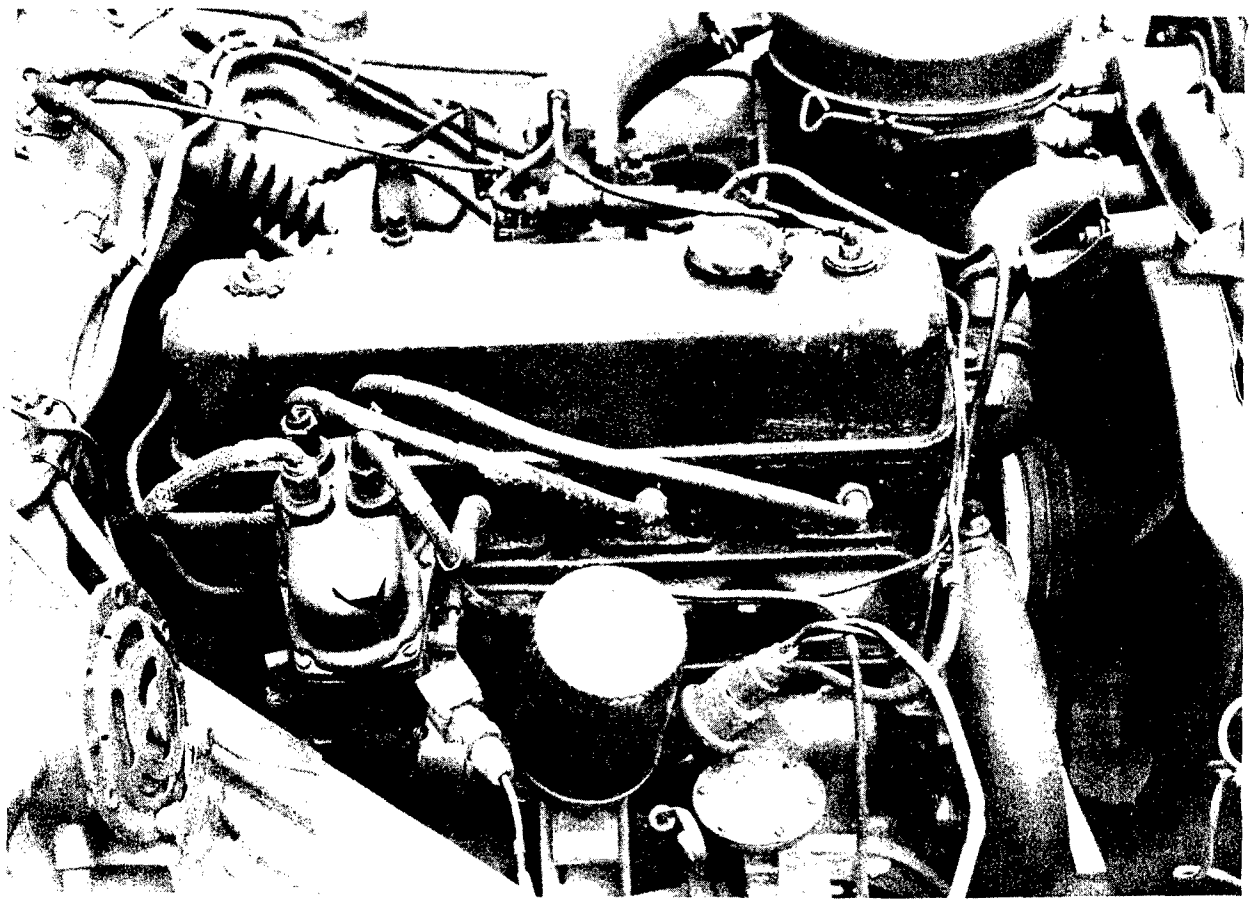

Figure 5.17

Holographic Field of View of M151 Engine. The Prominent Engine Components are: Top, Valve Cover; Left, Distributor; Center, Oil Filter; Right Bottom, Radiator Hose and Radiator.

Engine Holographic Series at 1050 RPM

Figures 5.18 through 5.21 represent a series of double exposure holograms taken of the right side of the M151 starting at a time t=0 which is synchronous which the number 1 cylinder spark plug pulse. The time interval between pulses was maintained at a constant 150 microseconds.

Each of these holograms represents some combination of rigid body and compliant motion. The engine is rocking on its motor mounts giving rise to a substantial amount of rigid body rotational motion which is indicated by the straight parallel fringes on the distributor, oil filter, and electrical cables. If the laser timing is such that a particular region on the engine is near the point of its maximum rotational swing where the differential displacement is small during the time interval Δt, then the parallel fringes will be rather widely spaced. Since the various engine components have rotational motion with varying amplitude and phases, then the parallel fringe patterns will generally be quite distinct. A sequence of holograms taken at different times during the firing sequence will provide enough information to determine the magnitude of the rotational phase between various components.

The curvature of the holographic fringe patterns on the engine is generally due to compliant or deformation type motion. The valve cover is a classic example as are the radiator hose and the spark plug cables. The spark plug cables are particularly interesting since the curved bending fringes are between parallel fringe patterns indicating the location of a potential fatigue area caused by mechanical bending stresses.

Figure 5.18

Engine Speed: 1050 RPM. Holographic Illumination Just Before the Firing of the #1 Spark Plug, t=0 ms.

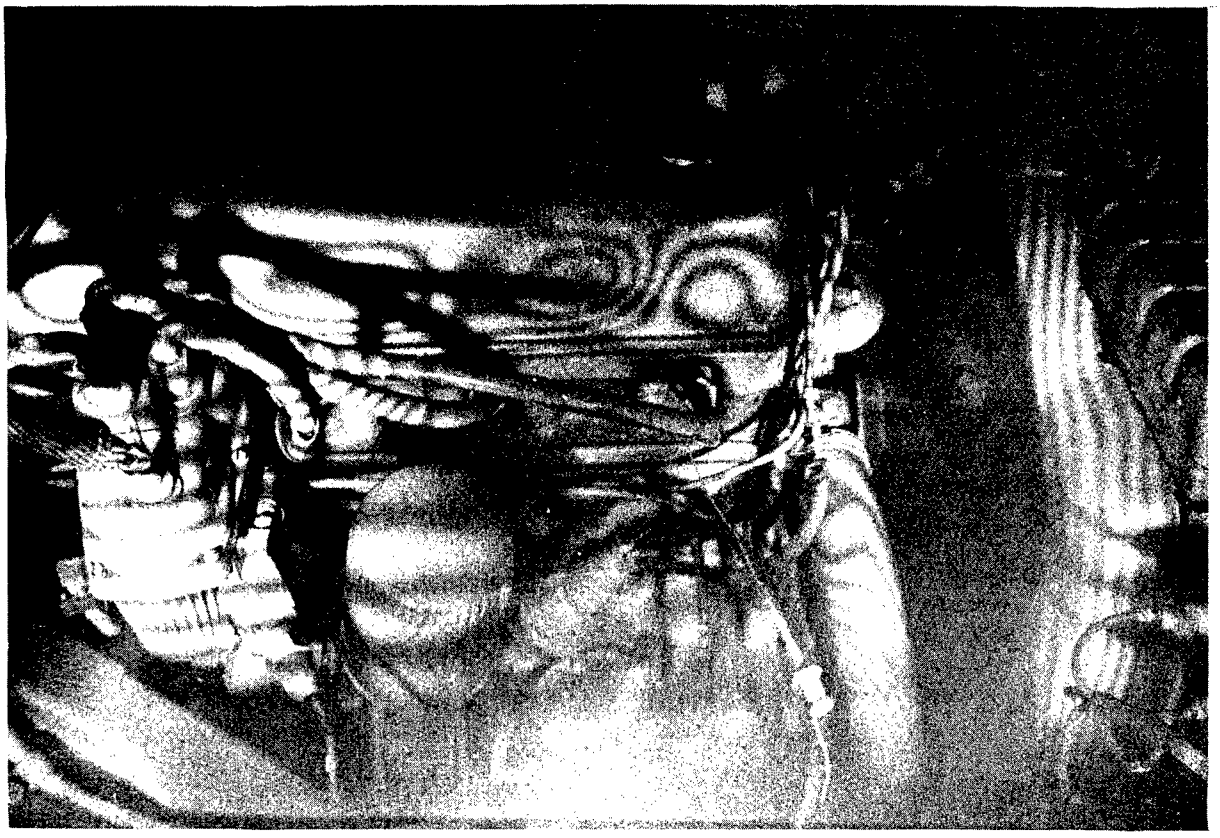

Figure 5.19

Engine Speed: 1050 RPM. Holographic Illumination During the Firing of the #1 Spark Plug, T=30 ms.

Figure 5.20
Engine Speed: 1050 RPM, t=60ms

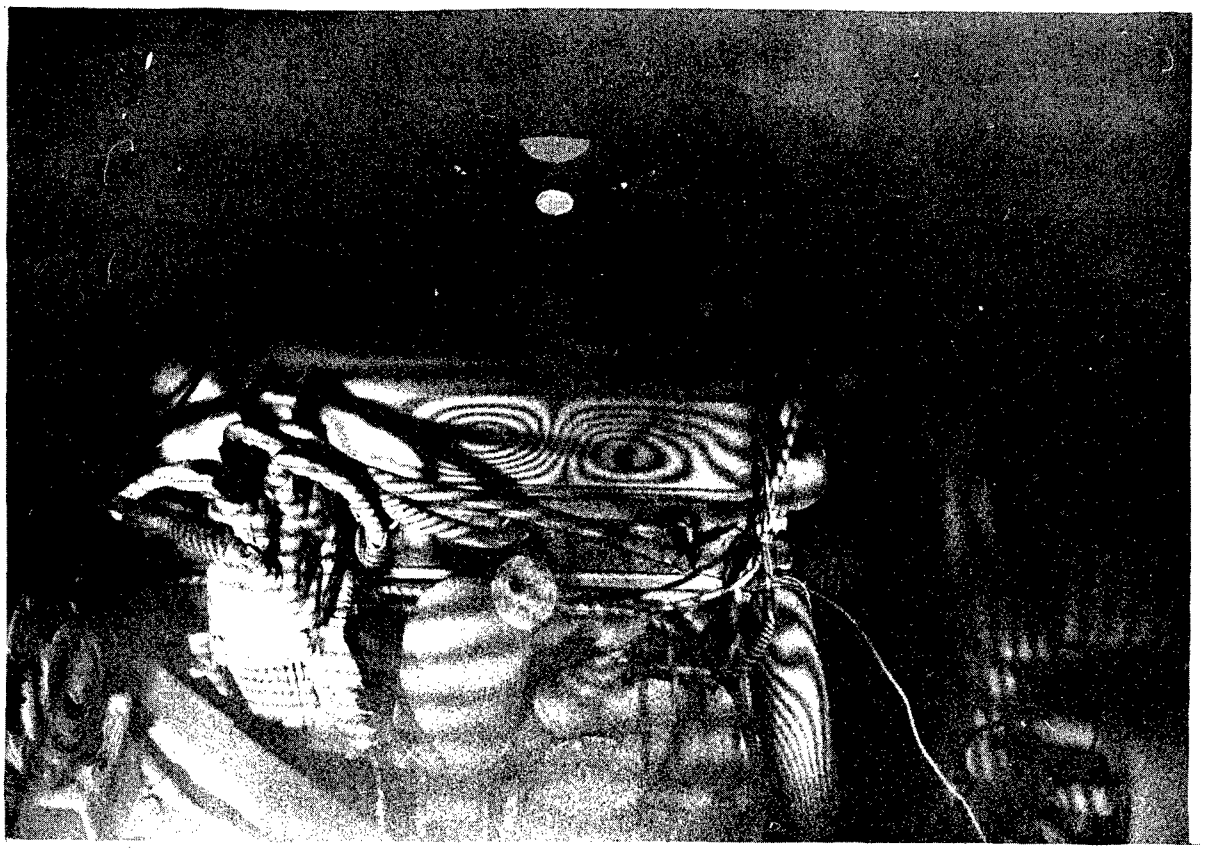

Figure 5.21
Engine Speed: 1050 RPM, t=100ms

Engine Holograpgic Series at 2000 RPM

Figures 5.22 through 5.27 represent a series of holograms taken when the engine is running at 2000 RPM for a pulse separation time of 150 micro-seconds. As expected an increase in engine RPM results in larger fringe densities and displacement amplitudes.

The flexural fringes on the radiator hose represent an interesting effect. The excitation frequencies which are present at an 2000 RPM engine speed generate an anti-resonance condition on the hose itself. The broadly spaced fringes both parallel and perpendicular to the length of the hose represent a significant nodal point of vibration which occurs at 2000 RPM and not 1000 RPM.

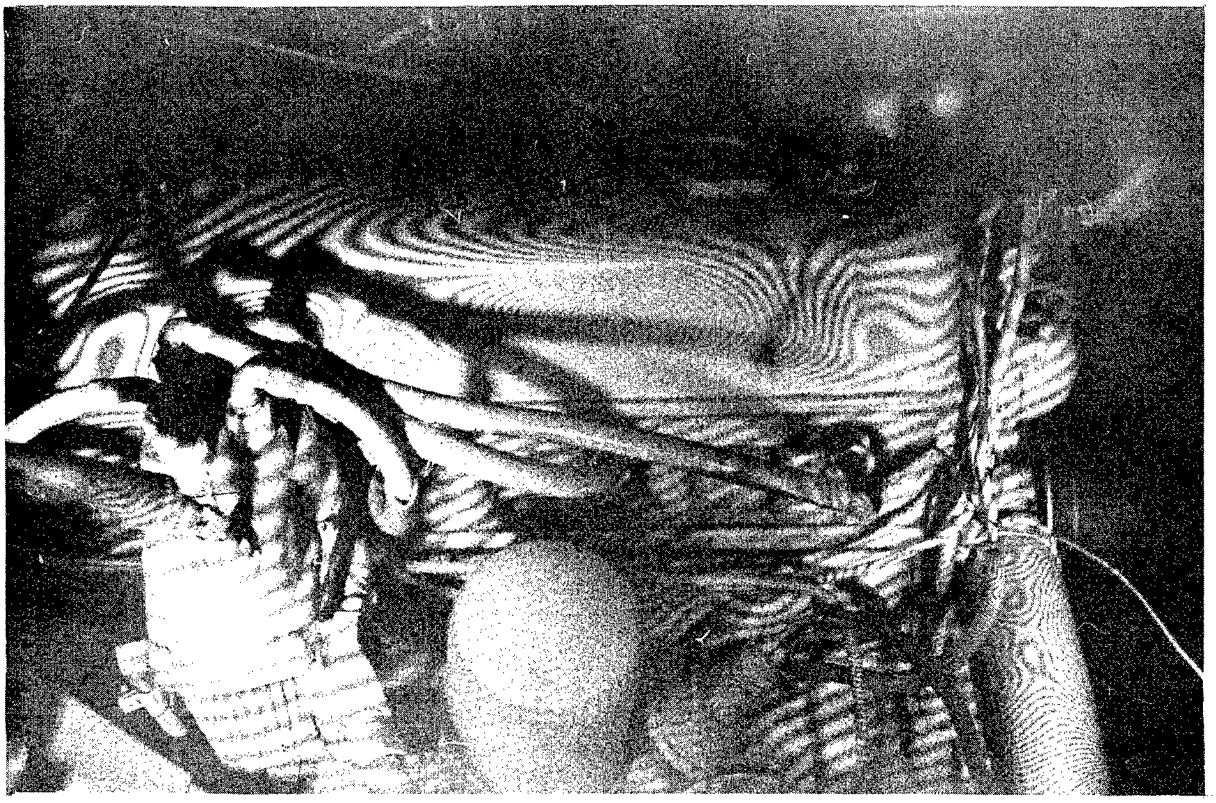

Figure 5.22
Engine Speed: 2000 RPM t=0ms

Figure 5.23
Engine Speed: 2000 RPM t=7ms

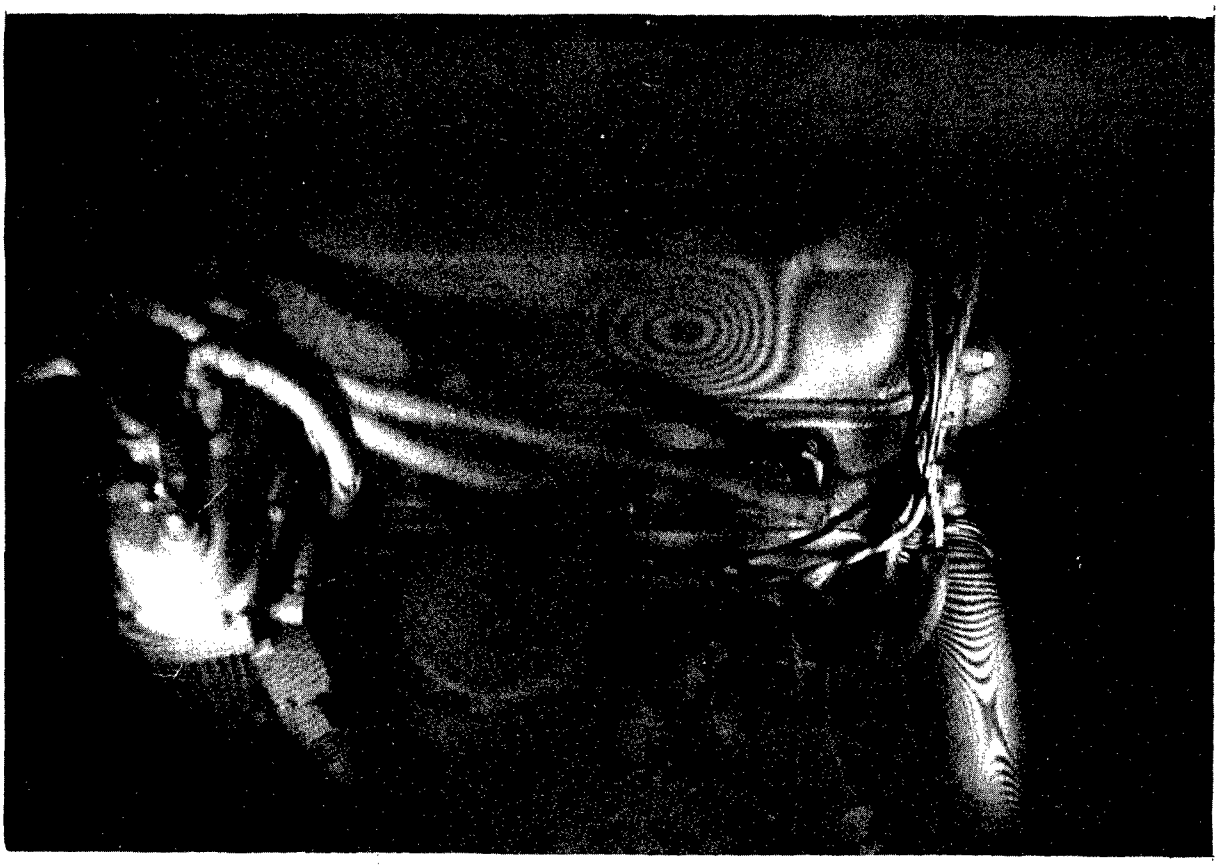

Figure 5.24

Engine Speed: 2000 RPM t=10ms. A Distinct Feature is the Saddle Point due to Bending Motion of the Radiator Hose.

Figure 5.25
Engine Speed: 2000 RPM t=15ms

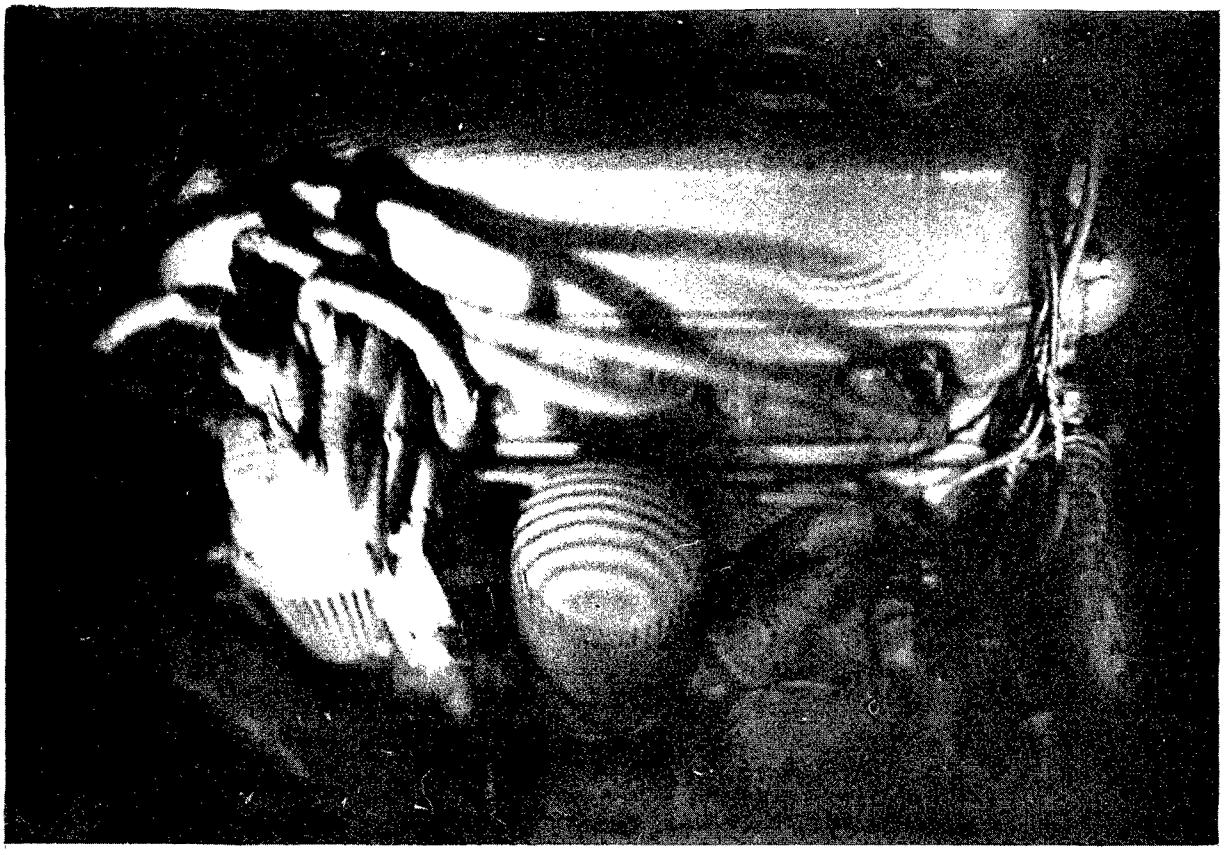

Figure 5.26
Engine Speed: 2000 RPM t=17ms

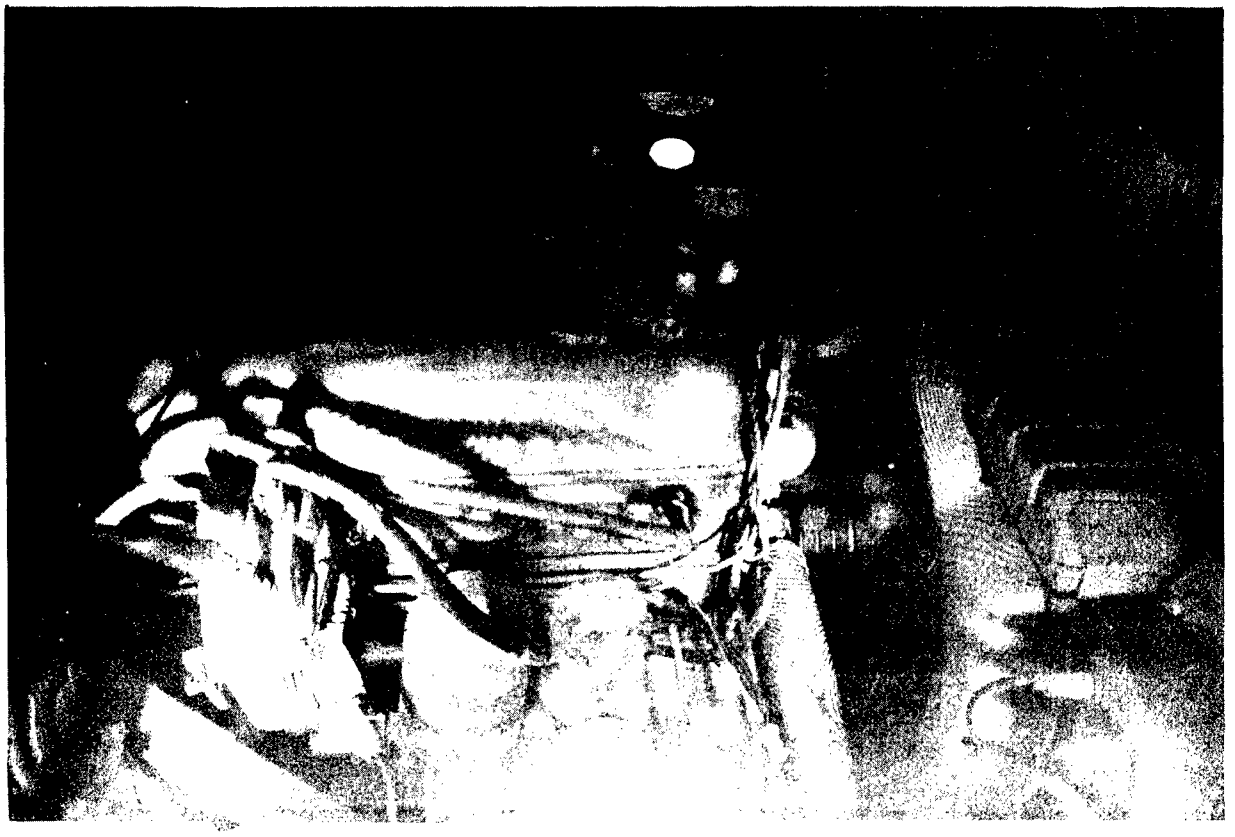

Figure 5.27

Engine Speed: 2000 RPM t=25ms. (#3 Spark Plug is Disabled)

Engine Holographic Series at 3000 RPM

Figures 5.27 through 5.30 are a sequence of double pulse holograms which were taken at an engine speed of 3000 RPM. Note again the large flexural bending node on the radiator hose. The compliant motion fringes on the valve cover are generally more complicated in shape and more fringes orders are visible on all engine components because of the larger displacement amplitudes.

Figure 5.28

Engine Speed: 3000 RPM t=0ms

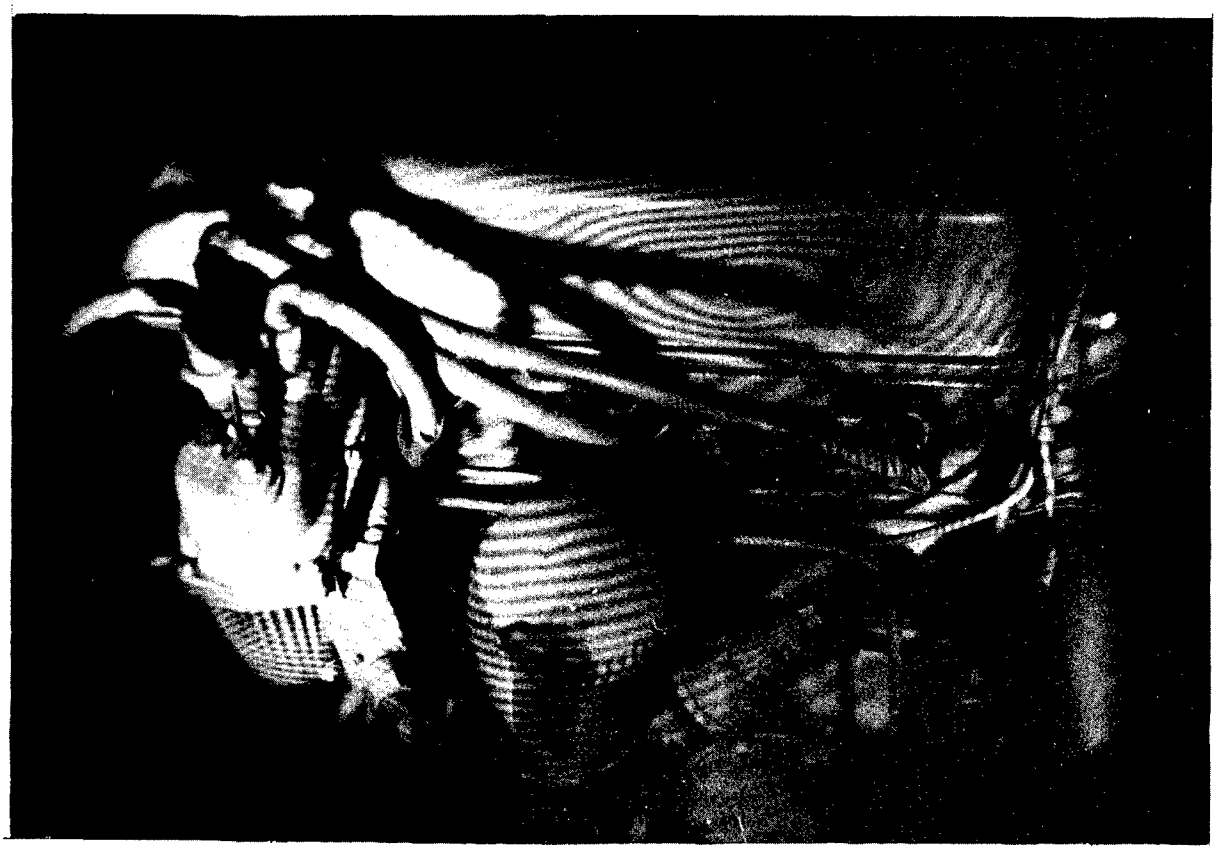

Figure 5.29
Engine Speed: 3000 RPM t=15ms

Figure 5.30
Engine Speed: 3000 RPM t= 30ms

Driver's Door Panel on the M151 (Jeep) with the Engine Running at 3000 RPM

Figures 5.31 through 5.35 are a series of double exposure holograms of the thin sheet metal door on a winter cab kit for the M151 (jeep) vehicle. The original hologram contained an image of the entire left side or driver's side of the vehicle while the photograph of the holographic image contains the door itself with dimensions of 49 in. X 44 in. Several notable features of these holograms include the discontinuities in the fringe patterns at the space between the edge of the door and the body of the vehicle, and the large circular bull's eye fringe patterns on the door itself which are regions of relatively large fringe density are unconstrained by the fixturing in the door while the regions with broad fringe patterns are well constrained and relatively stiff. Since the period of vibration for these holograms is generally much longer than the pulse separation time Δt between pulses, the fringes patterns are proportional to velocity rather than displacement and are important data for determining acoustic sound radiation from these moving surfaces.

Figure 5.31

Driver's Door, Engine Speed: 3000 RPM, t=0, t=150 Microseconds. The Outline of the Door, Frame and Gas Caps are Readily Visible. Each Structure is Characterized by its Unique Fringe Pattern. A Fine Fringe Structure Indicates a Large Relative Displacement.

Figure 5.32

Driver's door, Engine Speed: 3000 RPM, t = 3ms. This Hologram was taken shortly after the #1 Cylinder Firing.

Figure 5.33
Driver's Door, Engine Speed: 3000 RPM t=6ms

Figure 5.34

Driver's Door, Engine Speed: 3000 RPM, t=10ms.
The Firing Time of #3 Cylinder

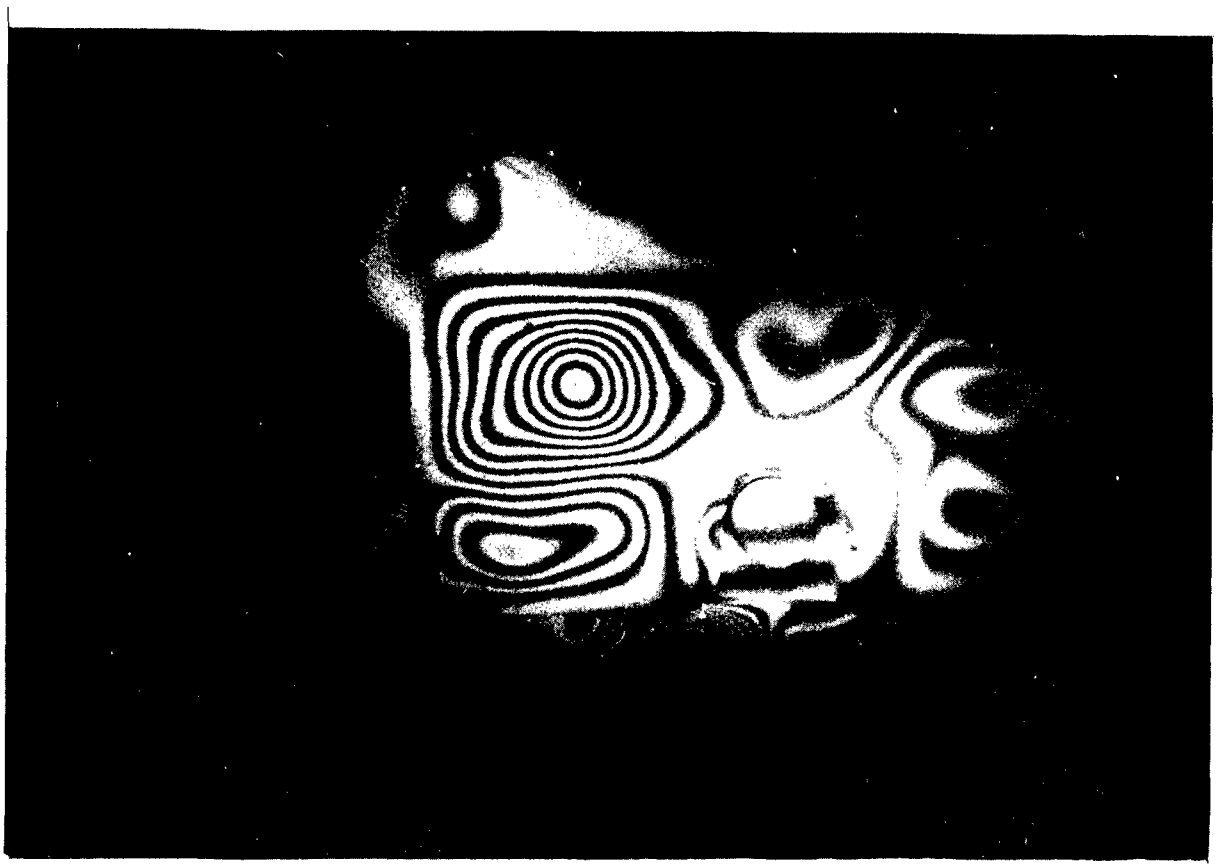

Figure 5.35

Driver's Door, Engine Speed: 3000 RPM, t=14ms. This Pattern is Almost Similar to Figure 50 at the Beginning of the Firing Sequence. Notice the Re-appearance of the Fringe Pattern on the Gas Cap.

A series of holograms have been taken of the M151 vehicle relative to the engine firing sequence as illustrated in Figure 5.15. The number one spark plug firing pulse is monitored inductively as described in Figures 3.9 through 3.11. A typical procedure is to operate the engine at some constant RPM level and adjust the delay in the laser triggering circuit to a preset value. These delay times correspond to a relative shift between 0^{o} and 720^{o}. The entire motion of a particular vehicle component can be represented at a particular RPM value from a sufficiently large sequence of holograms.

Figure 5.16 illustrates the orientation of the pulse laser holocamera relative to the engine compartment in the M151 vehicle. Figure 5.17 is a close-up view of the engine from the perspective of the holographic plate.

Figures 5.18 through 5.30 represent three sequences of holograms of the M151 engine running at 1,050 RPM, 2,000 RPM and 3,000 RPM. From a visual inspection of the holograms, a number of engine components can be easily identified such as the distributor, oil filter, valve cover, radiator hose, fan housing and spark plug cables. The complexity and diversification of the automotive engine presents a difficulty in analyzing such structures for mechanical integrity. In contrast, the vibration configuration on a flat surface generated by the engine running at 3,000 RPM, Figures 5.31 through 5.35, illustrates the development of more well-known classical modal structures.

From these series of holograms of a typical automotive structure, it is apparent that double pulse holography has the capability of recording important information about local vibration amplitudes in terms of fringe contours and density. Areas on structures or components which may be susceptible to fatigue would be identified by large fringe densities particularly at stressed locations, such as bends or joints. This technique, when used in conjunction with other interferometric methods and computer modal analysis, can be quite valuable in analyzing potential fatigue problems early in the prototype development stages.

6. HOLOGRAPHY INTERFEROMETRY

6.1 Theory

A schematic diagram of a typical holographic setup is illustrated in Figure A.1. The laser beam illuminates the object at O and the holographic plate is positioned at Q. The diffracted light from the object surface P produces a Fresnel hologram at the film plane Q. The interference pattern which is formed by the object and reference beams produces the holographic image at Q.

The optical field which is recorded on the holographic plate is proportional to

$$C|R + O|^2 = C|R|^2 + C|O|^2 + CR^*O + CRO^* \qquad (6.1)$$

where C is the illuminating wave, R is the reference wave, and O is the object wave. The third term in Equation 6.1 is proportional to the original object. A holographic image reconstruction produces a virtual image of the object if the holographic plate is illuminated by another laser beam R. The term RR^*O is now proportional to the object beam O via the real function R^*R. Since R and O may be functions of time during the exposure interval, the third term in Equation 6.1 is a sum of incremental contributions:

$$W = A\int R^*O\,dt \qquad (6.2)$$

where the time integration is over the exposure interval and the constant A depends on C, the exposure time, and the properties of the recording medium. The relative irradiance is

$$I/I_o = |W|^2/|W_o|^2 \qquad (6.3)$$

where W is the primary reconstructed wave for the moving object, W_o is the primary reconstructed wave for a stationary object, and I and I_o are the corresponding irradiances.

6.2 Uniform Motion

The object motion will degrade the holographic images and this degradation can be used to analyze the motion. This analysis technique is called holographic interferometry if the interference fringes are formed on the object and can be used to measure small changes in the motion of complex three-dimensional objects. The object motion generates a complex phase factor for the optical path difference d:

$$O = O_o \exp(jKd_o) \qquad (6.4)$$

where $K = 2\pi/\lambda$ and d_o may be a function of time. The above analysis assumes that the reference and object beams are matched to within the temporal coherence length of the source laser.

Figure 6.1 illustrates the geometrical considerations for the holography of moving objects. The displacement $\vec{d}_o$ for this example is perpendicular to the surfaces $z(t_2)$ and $z(t_1)$. The angles α and β are the respective orientations of the object and reference beams relative to the displacement vector $\vec{d}_o$ is

$$d_o = v_o \Delta t \qquad (6.5)$$

where v_o is the average velocity of the planar object surface during the time interval $t_2 - t_1 = \Delta t$. The rays O_1 and O_2 correspond to the optical paths of the object beam at times t_1 and t_2. The path length difference d between O_1 and O_2 is

$$d = d_o\ (\cos\alpha + \cos\beta) = v\Delta t\ . \tag{6.6}$$

A more detailed derivation of the result in Equation 6.6 can be found in Appendix A1.

The illumination of the object with a single rectangular pulse of duration T for a uniform motion $d_o = v_o\Delta t$ is given by the expression

$$\begin{aligned} W &= A\int_o^T \exp(jKvt)dt \\ &= AT(\exp[jKvT]-1)/jKvT \end{aligned} \tag{6.7}$$

Since $|W_o|^2 = A^2T^2$, the relative irradiance is

$$\begin{aligned} I/I_o &= (\sin^2 k_2 vT/2)/(k_2 vT/2)^2 \\ &= \operatorname{sinc}^2(\pi vT/\lambda). \end{aligned} \tag{6.8}$$

Equation 6.8 is a well know function which has zeros that occur at $v\ T/\lambda = 1,2\ \ldots$ and these zeros correspond to dark fringes that form contours of equal velocity.

Although a rectangular pulse shape may be realistic for a chopped continuous wave laser, Q-switched pulsed lasers have an approximately Gaussian intensity profile which is proportional to $\exp[-4\ln 2(t/T)^2]$, where T is the full pulse width at half maximum power. The quantity W for uniform motion and a Gaussian intensity profile is

$$\begin{aligned} W &= A\int_{-\infty}^{\infty} \exp[-4\ln 2(t/T)^2]\exp(jKvt)dt \\ &= (AT/2)\ \sqrt{\pi/\ln 2}\exp[-K^2v^2T^2/16\ \ln\ 2]\ . \end{aligned} \tag{6.9}$$

Since $|W_o|^2 = \pi T^2A^2/\ln 2$, the relative irradiance is

$$\begin{aligned} I/I_o &= \exp[-k^2v^2T^2/8\ \ln 2] \\ &= \exp[-\pi^2(vT/\lambda)^2/2\ln 2]. \end{aligned} \tag{6.10}$$

The equation 6.10 is a function of the parameter vT/λ where v is the velocity of the object surface during the pulsed illumination, T is the half-power pulse width, and λ is the wavelength of the laser light source. The parameter T is approximately 20 nsec for a Q-switched ruby laser; consequently, the factor vT/λ satisfies the following equation:

$$vT/\lambda << 1 . \tag{6.11}$$

The quantity I/I_o is approximately equal to one, and the Gaussian pulse approximates quite well a narrow rectangular laser pulse.

If two or more narrow pulses are used with a constant pulse separation, then velocity fringes are formed for uniformly moving objects. Consider now a hologram where a series of N pulses illuminates the object, and each pulse is separated by a constant time interval S with a rectangular shape and an infinitesimal pulse width. The reconstructed wave W is described by the following expressions:

$$\begin{aligned} W &= A\int_{-\infty}^{\infty} \sum_{n=0}^{n-1} \delta(t-nS)\exp(jkvt)dt \\ &= A \sum_{n=0}^{n-1} \exp(jnkvS) . \end{aligned} \tag{6.12}$$

This geometric series is summed so Equation 6.12 becomes

$$W = A(\sin NkvS/2)/\sin kvS/2 . \tag{6.13}$$

Since $|W_o|^2 = N^2A^2$, the relative irradiance becomes

$$I/I_o = [\sin^2\pi N(vS/\lambda)]/N^2\sin^2(\pi vS/\lambda) . \tag{6.14}$$

When N=2, then

$$I/I_o = \tfrac{1}{2} + (\tfrac{1}{2})\cos 2\pi vS/\lambda \tag{6.15}$$

for narrow rectangular pulses. This form for the irradiance function is the classic double pulse interferogram where the object displacement between pulses is vS.

6.3 Uniform and Vibration Motion

The optical path difference for an object undergoing a combination of uniform and sinusoidal motion simultaneously is $d = vT + \ell \sin\omega t$ where ℓ and ω are the amplitude and frequency of vibration. The quantity W for a single pulse of infinite duration is

$$W = A\int_{-\infty}^{\infty} \exp[-4\ln 2(t/T)^2]\exp[jk(vt+\ell\sin\omega t)]dt \qquad (6.16)$$

This equation can be rewritten using a series expansion of $\exp[jk\ell\sin\omega t]$ in terms of the nth order Bessel functions $J_n(k\ell)$:

$$\begin{aligned} W &= A\int_{-\infty}^{\infty} \exp[-4\ln 2(t/T)^2 \exp(jvt) \sum_{n=-\infty}^{\infty} J_n(k\ell)\exp(jn\omega t)dt \\ &= (AT/2)\sqrt{\pi/\ln 2}\sum_{n=-\infty}^{\infty} J_n(k\ell)\exp[-(kv+n\omega)^2T^2/16\ln 2]. \end{aligned} \qquad (6.17)$$

If the vibration period $(\omega/2\pi)^{-1}$ is small compared to the pulse width ($\omega T>>1$) and the object velocity is much less than one wavelength per vibration period ($kv<<\omega$), then Equation 6.17 becomes

$$W = (AT/2)\sqrt{\pi/\ln 2}\, J_o(k\ell)\exp[-k^2v^2T^2/16\ln 2]. \qquad (6.18)$$

Since $W^2 = \pi^2A^2T^2/4\ln 2$, the relative irradiance is

$$\begin{aligned} I/I_o &= J_o^2(k\ell)\exp[-k^2v^2T^2/8\ln 2] \\ &= J_o^2(2\pi\ell/\lambda)\exp[-\pi^2(vT/\lambda)^2/2\ln 2]. \end{aligned} \qquad (6.19)$$

The quantity I/I_o is plotted in Figure 6.2 as a function of ℓ/λ. The relative irradiance function is proportional to J_o^2, and whose zeros correspond to dark fringes that form contours of constant vibration amplitude. These fringes are identical to those from time average holographic interferometry which uses shuttered continuous wave lasers. The time average technique is suitable for the study of nodal patterns on standing wave vibration phenomena since the higher order maxima or bright fringes decrease in intensity as a function of increasing displacement amplitude.

6.4 Double Pulse Holographic Interferometry

Figure 6.1 illustrates the general optical configuration for a double pulse hologram. The two laser pulses are approximately 30 nanoseconds in duration and this value is much less than the vibration period $(\omega/2\pi)^{-1}$. The laser beam illuminates the diffuse object surface at two instants in time t_1 and t_2. The reflected light interferes with the reference beam in the holographic plate.

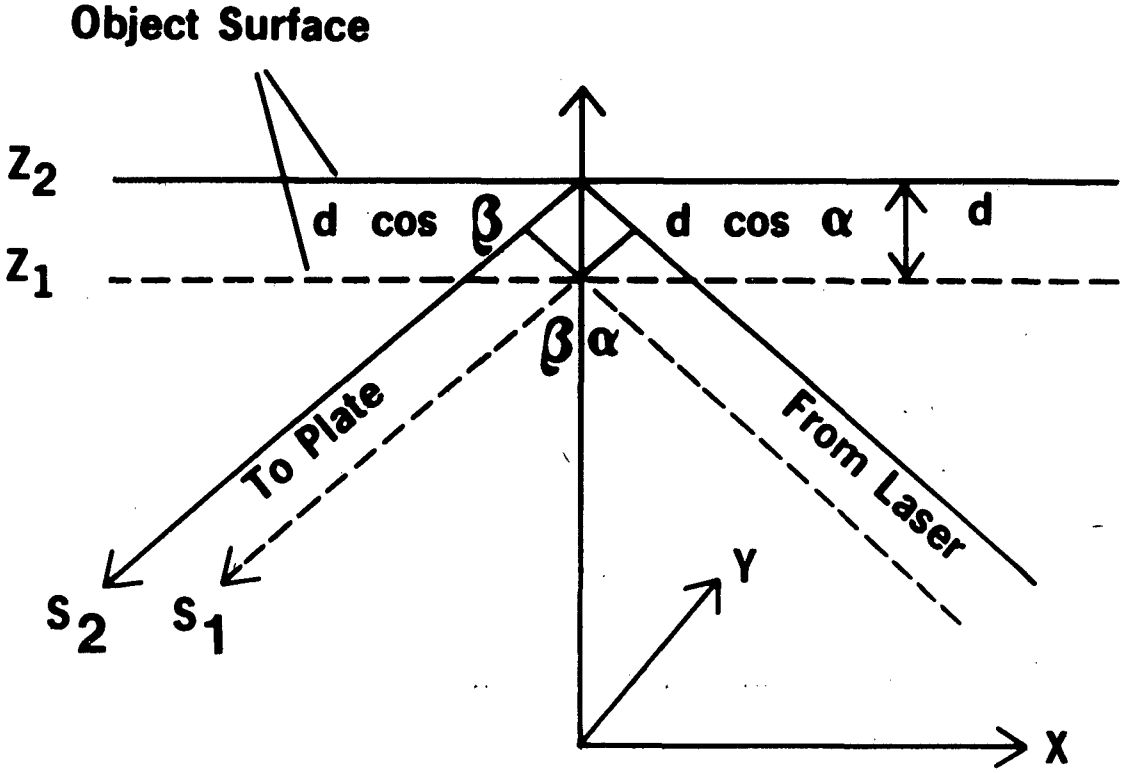

FIGURE 6.1

A schematic representation of a flat surface at positions Z_1 and Z_2 during times t_1 and t_2. The path lengths of the two lasers pulses are designated by the rays S_1 and S_2.

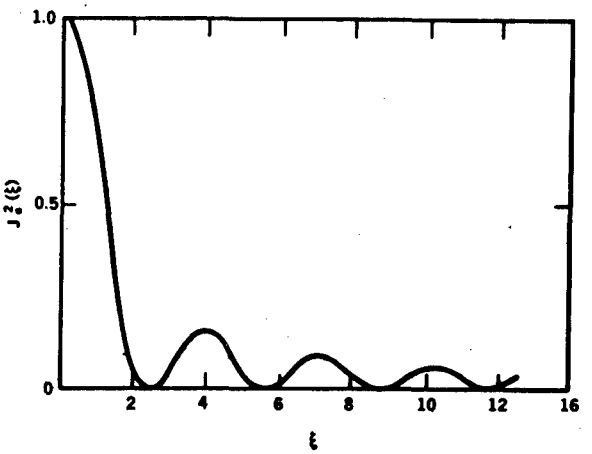

FIGURE 6.2

The relative irradiance function I/I_o for time average holography is proportional to $J_o^2(\xi)$ where ξ is the normalized displacement amplitude of the sinusoidal displacement.

The object rays O_1 and O_2 have the same amplitude $|O_1|$:

$$\begin{aligned} O_1 &= |O_1|\exp i\phi_1 \\ O_2 &= |O_1|\exp i(\phi_1+\Delta\phi) \end{aligned} \tag{6.20}$$

where O_2 is phase shifted by $\Delta\phi$ compared to O_1 because of the object motion. Equation 6.1 gives the recorded intensity pattern for a square law detection as

$$I/I_o = |O_1+O_2|^2 = 4|O_1|^2\cos^2\Delta\phi/2 \; . \tag{6.21}$$

The condition for an intensity minima in Equation 6.21 is

$$\begin{aligned} \Delta\phi &= (2n+1)\pi \qquad n=0,1,2 \ldots \\ &= d_o(\cos\alpha+\cos\beta)2\pi/\lambda \\ &= 2\pi d/\lambda. \end{aligned} \tag{6.22}$$

Equation 6.22 can be solved to yield

$$d_o = (2n+1)\lambda/2(\cos\alpha+\cos\beta) \qquad n=0,1,2 \ldots \tag{6.23}$$

The minima (dark fringes) are at points where the displacement d_o satisfies Equation 6.23. The relative intensity maxima occur when d_o satisfies the following equation:

$$d_o = n\lambda/(\cos\alpha+\cos\beta) \qquad n=0,1,2, \ldots \tag{6.24}$$

The above formulation will only yield the relative change in the displacement d_o between two points on the object surface during the time interval Δt. The absolute vibration amplitude at a single point on the object surface is determined by counting light or dark fringes from a reference point of zero motion (n=0). This zero motion information must be determined by some other means such as accelerometer data, etc. The zero motion or zero amplitude regions are always bright fringe areas, however, all bright fringes have the same intensity for pulse holograms as opposed to the J_o^2 intensity modulation for time average continuous wave holograms. The relative phase of the two laser pulses for the sinusoidal object surface motions must also be known to determine the absolute vibration amplitude. Figure 3.13 illustrates this timing sequence using an accelerometer at a single point on the object surface.

The lower curve in Figure 6.3 is a graph of acceleration as a function of time for a simple sinusoidal motion

$$a(t) = -A\omega^2 \sin\omega t \tag{6.25}$$

where A is the amplitude and ω is the radial frequency. The function a(t) can also be integrated twice to yield the displacement function

$$z(t) = A\sin\omega t \tag{6.26}$$

which corresponds to the upper curve in Figure 6.3.

The displacement d_o between the two laser pulses is

$$\begin{aligned} d_o &= z(t_2)-z(t_1) \\ &= A(\sin\omega t_2-\sin\omega t_1). \end{aligned} \tag{6.27}$$

The quantity d_o is also equal to

$$d_o = (2n+1)\lambda/[2(\cos\alpha+\cos\beta)]. \tag{6.28}$$

Equations 6.27 and 6.28 can be solved to yield the amplitude function

$$A = (2n+1)\lambda/[2(\cos\alpha+\cos\beta)(\sin\omega t_2-\sin\omega t_1)]. \tag{6.29}$$

This number n is determined by counting the dark fringes between the zero motion or nodal point and the accelerometer measurement point. This procedure calibrates the amplitude function A for all points in the immediate vicinity of the accelerometer.

7. MEASUREMENT OF STRESS-STRAIN PARAMETERS

The vector displacement $\vec{L} = \vec{i}L_x + \vec{j}L_y + \vec{k}L_z$ at each point on an opague, diffusely reflecting object can be measured using holographic interferometry. The deformation of test objects can be used to determine the stress, strain, and bending moments. The strain is related directly to the derivatives of the displacement while stress and bending moments are inferred from strain measurements via the constitutive equations of the material. The Hooke's law of elasticity and the corresponding elastic constants are used for linear or elastic materials.

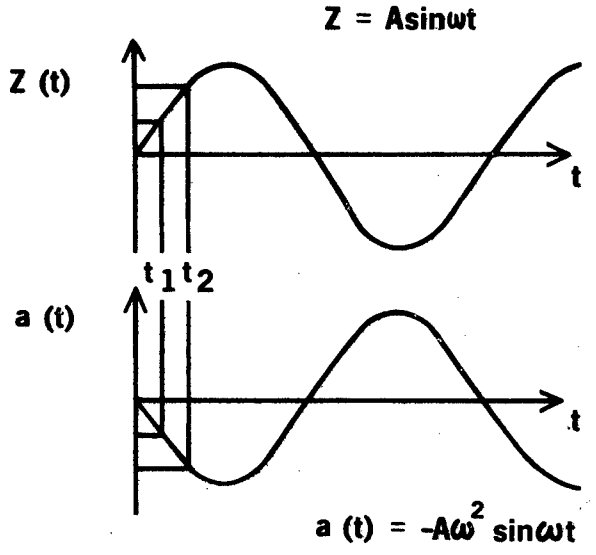

FIGURE 6.3

The bottom graph represents acceleration as a function of time as measured by an accelerometer on the object. The top curve represents the corresponding displacement function.

The mechanical strain is calculated by differentiating displacement measurements which are determined by fringe localization observations. A standard notation is adopted to use U,V,W in preference to L_x, L_y, L_z for the displacement vector at a point x,y,z on the object. The strain tensor is a quantity which contains nine components. Six of these components are independent and they consist of three uni-axial strain components and three shear strain components. These tensor components are defined mathematically as

$$\begin{aligned} \varepsilon_x &= \partial_x U \\ \varepsilon_y &= \partial_y V \\ \varepsilon_z &= \partial_z W \\ \gamma_{xy} &= (\partial_y U + \partial_x V)/2 \\ \gamma_{yz} &= (\partial_z V + \partial_y W)/2 \\ \gamma_{zx} &= (\partial_x W + \partial_z U)/2 \end{aligned} \qquad (7.1)$$

where the ε's are the uni-axial strain components and the γ's are the shear strain components for infinitesimal displacements. The uni-axial strain components are the change in length per unit length of a small element of material along each coordinate direction. The shear strains are related to a decrease in angle between two line segments of material points which were initially parallel to the coordinate directions.

Holographic interferometry does not provide sufficient information to evaluate all of the derivatives in Equation 7.1. Three independent fringe observations yield three independent components of displacement U(x,y), V(x,y), and W(x,y) on the surface. This information is sufficient to calculate the in-plane strain components ε_x, ε_y, and γ_{xy} in the object surface and the in-plane rotation ω_z about an axis normal to the surface where

$$\begin{aligned} \omega_x &= (\partial_y W - \partial_z V)/2 \\ \omega_y &= (\partial_z U - \partial_x W)/2 \\ \omega_z &= (\partial_x V - \partial_y U)/2 \end{aligned} \qquad (7.2)$$

are the infinitesimal rotational object motions. Holographic interferometry does not provide a complete specification of all six strain components in Equations 7.1 and 7.2. The derivatives of displacement with respect to the coordinate which is normal to the surface are not determined, consequently, only three of the six independent strain components are determined from the fringe analysis techniques. The knowledge of the displacement components U(x,y), V(x,y) and W(x,y) is sufficient to describe the special case of plane strain.

8. RIGID BODY MOTION

Rigid body motion is an important example of fringe formation and localization. The most general rigid body motion consists of a translation and a rotation. The quantities L_x, L_y and L_z are constant at all points on the object surface so that the derivatives L_i where i,j = 1, 2, 3 are equal to zero. The denominator of Equation B.9 is equal to zero and the fringes localize at z=∞. These fringes are observed with good visibility only at infinity and in the back focal plane of a lens. If the illumination beam is spherical, then the unit vector $\vec{K}_1$ is not constant and curvature effects are not negligible if the point source is sufficiently close to the object.

Consider the example where the object motion is purely translational. The assumptions are made that the vector $\vec{K}_1$ is constant over the object and that the illumination beam is a collimated source. The fringes localize at infinity and the basic phase shift is $\Delta\phi = 2\pi(\vec{K}_2-\vec{K}_1)\cdot\vec{L}$. The equation for bright fringes is

$$K_x L_x + K_y L_y + K_z L_z = N\lambda \qquad N = 0, 1, 2, \ldots \tag{8.1}$$

If the object motion of a double exposure hologram is a translation parallel to the surface, then the fringes are perpendicular to the surface displacement vector $\vec{L}$. The phase difference

$$\Delta\phi = 2\pi(K_{2x} - K_{1x})L_x/\lambda \tag{8.2}$$

is a constant for all ray pairs leaving the surface with a value of K_{2x}. If a lens is placed one focal length f from the object surface, then the fringe spacing d_f in the back focal plane is

$$d_f = \lambda f/L_x \tag{8.3}$$

No fringes are visible if $\vec{K}\cdot\vec{L} = 0$. This condition implies that the displacement $\vec{L}$ is perpendicular to the sensitivity vector $\vec{K}$.

A translation of the object normal to the surface gives rise to circular fringes of equal inclination. The phase difference

$$\Delta\phi = 2\pi(K_{2z}-K_{1z})L_z/\lambda \tag{8.4}$$

is constant for all ray pairs which are paralled to a specific direction where, for simplicity, we consider $K_{2y} = 0$. A phase shift of 2πm gives

$$K_{2z} = K_{1z} + m\lambda/L_z \tag{8.5}$$

Since $\vec{K}_2$ is a unit vector

$$K_{2x}^2 + K_{2z}^2 = 1 \tag{8.6}$$

so
$$K_{2x} = \{1 - [K_{1z} + m(\lambda/L_z)^2]\}^{\frac{1}{2}} \tag{8.7}$$

The quantity $m\lambda/L_z$ is generally small compared to K_{1z} so that

$$K_{2x} \tilde{=} [1-K_{1z}^2 - 2mK_{1z}\lambda/L_z]^{\frac{1}{2}} \tag{8.8}$$

The center fringe for which $K_{2x} = 0$ is

$$m_o = L_z(1-K_{1z}^2)/(2K_{1z}\lambda). \tag{8.9}$$

The nth fringe is at a radius r_f from the center of the focal plane and it is given by

$$r_f = fK_{2x} \tilde{=} f[2nK_{1z}\lambda/L_z]^{\frac{1}{2}}. \tag{8.10}$$

A third example of a rigid body motion is a rotation about the y axis on the object surface by a small angle θ. The displacement vector $\vec{L}$ is given by the approximate expressions

$$\begin{aligned} L_x &= 0 \\ L_y &= 0 \\ L_z &= \theta_x \end{aligned} \tag{8.11}$$

The localization conditions B.9 yield

$$\begin{aligned} z &= -K_{2x}K_{2z}^2 x/K_z \\ K_{2z}^2 K_{2y}^2 \theta X &= 0 \end{aligned} \tag{8.12}$$

where again it is assumed that $K_{2y} = 0$. The equations of the bright fringes are

$$K_z \theta X = N\lambda \tag{8.13}$$

where N=0,1,2,.., etc. Equations 8.12 are satisfied if $K_{2y} = 0$ and the fringes will then localize on the object surface. Generally an observer will see straight line fringes which are parallel to the axis of rotation when the object rotates about an axis on the surface. When the object rotates by an angle θ about an axis parallel but off of the surface, the fringes do not lie on the object surface.

A final example of fringe localization and analysis is the cantilever beam. The beam is assumed to be of length L with one end fixed rigidly to a massive object as shown in Figure 9.1. The x axis coincides with the original unbent position of the beam. The differential equation of the bent beam is

$$EI \frac{d^2y}{dx^2} = M. \tag{8.14}$$

The quantity M is the bending moment which is given by

$$M = -PL + Px \tag{8.15}$$

where P is the vertical reaction force.

A double integration of Equation 8.14 yields

$$EIy = -PLx^2/2 + Px^3/6 + C_1x + C_2 \tag{8.16}$$

where E is the modulus of elasticity and I is the moment of inertia of the cross section about the neutral axis. The conditions that dy/dx and y(x) vanish at x=0 imply that $C_1=C_2=0$. If the maximum deflection of y is given by

$$y(L) = d_o \tag{8.17}$$

then

$$d_o = \frac{-PL^3}{3EI}. \tag{8.18}$$

The vertical displacement y(x) is now

$$y(x) = d_o[3(x/L)^2 - (x/L)^3]/2. \tag{8.19}$$

The vector displacement $\vec{L}$ is

$$\vec{L} = d_o \hat{K}_z[3(x/L)^2 - (x/L)^3] = N\lambda \tag{8.20}$$

The equation for fringe localization is z=0 which corresponds to the fringes lying directly on the surface. The vector $\vec{K} = \vec{K}_1 - \vec{K}_2$ and the unit vectors $\vec{K}_1$, $\vec{K}_2$ are all normal to the surface.

9. Fringe Analysis of the Cantilever Beam

9.1 Cantilever Beam Fixture

A relatively simple fringe system to analyze is the cantilever beam which is shown in Figure 9.1a. The beam is fixed at one end while a static force is exerted normal to the beam at the other end. A double exposure hologram was taken of the cantilever beam with a continuous wave (CW) HeNe laser. The beam was displaced at its free end by an amount d_o as described in Eq. 8.19. A single exposure was taken before and after the displacement d_o to simulate a double pulse hologram of a cantilever beam which is vibrating in its simple bending mode with a frequency of 22Hz and an amplitude of 240μ. The same fringe pattern is generated with a static displacement of 6.6μ utilizing the CW double exposure method. The pulse method in this case dramatically reduces the measurement sensitivity which is important for large amplitude measurements.

The resulting CW fringe pattern for the beam displacement is graphically illustrated in Figure 9.1b. The zero motion light fringe corresponds to N=0, and it is located at the clamping point of the beam to the support fixture. The higher order fringes become more closely spaced as the beam deflection increases non-linearly according to Eq. 8.20.

9.2 Image Digitization

The fringe pattern in Figure 9.2 was scanned with a closed circuit TV (CCTV) camera and displayed on a monitor. The video rf signal was sampled by a video compression device which heterodynes the video signal down into the audio frequency range. Figure 9.4 is a photograph of the TV monitor with the line cursor and the audio signal superimposed on the cantilever beam image. This audio signal inputs a single scan line across the original fringe pattern into a Fast Fourier Transform (FFT) analyzer. Figure 9.3 is a block diagram of the digital circuitry for this data analysis instrumentation.

9.3 Fourier Analysis

A single line scan of the holographic fringe pattern in Figure 9.4 is shown in Figure 9.5. This time domain segment quite clearly has a periodic component which is modulated by some envelope function. The general form for this intensity pattern can be obtained from Eq. 6.21 and has the following expression:

$$I/I_o = A(t) + B(t)\cos\Delta\phi \qquad 9.1$$

FRINGE SYSTEM

FIGURE 9.1A

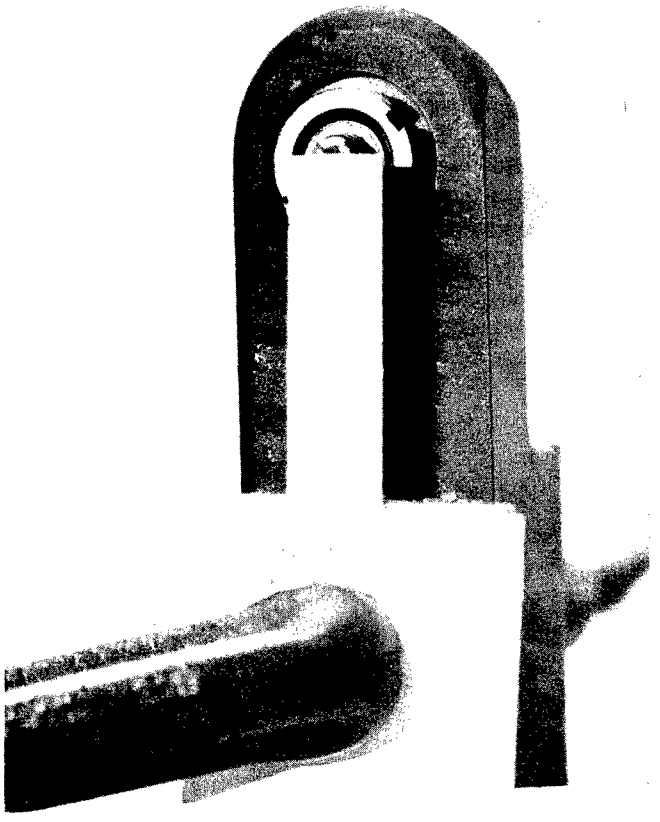

FRINGE PATTERN EXAMPLE

FIGURE 9.1B

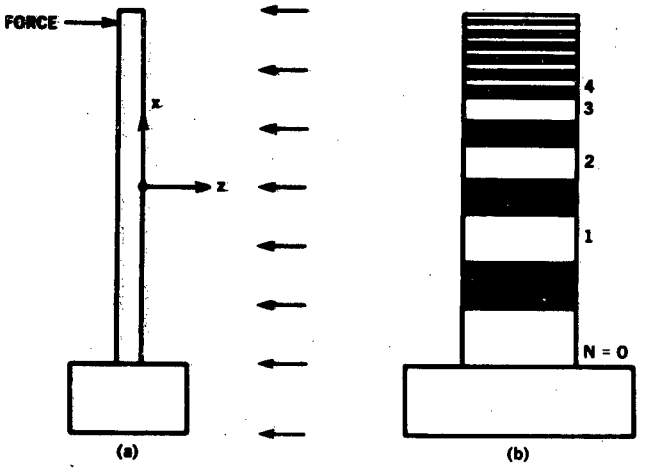

CANTILEVER BEAM FRINGE PATTERN

FIGURE 9 2

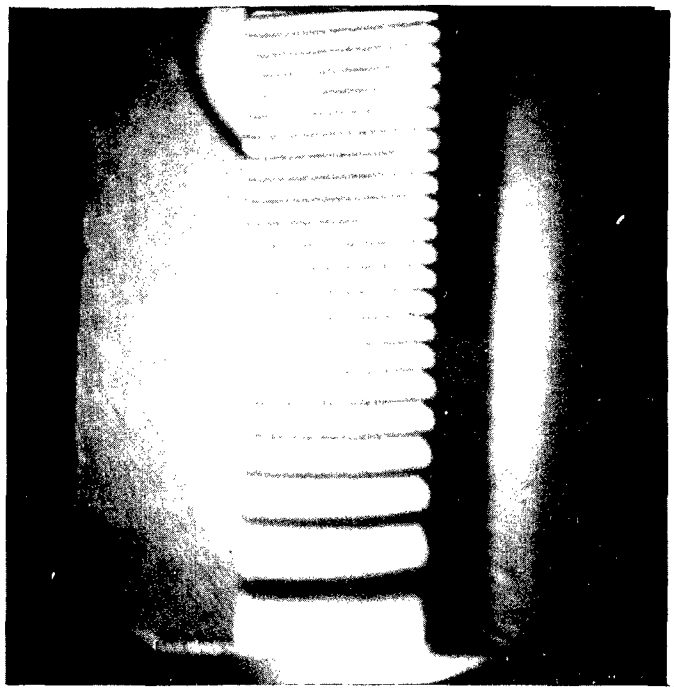

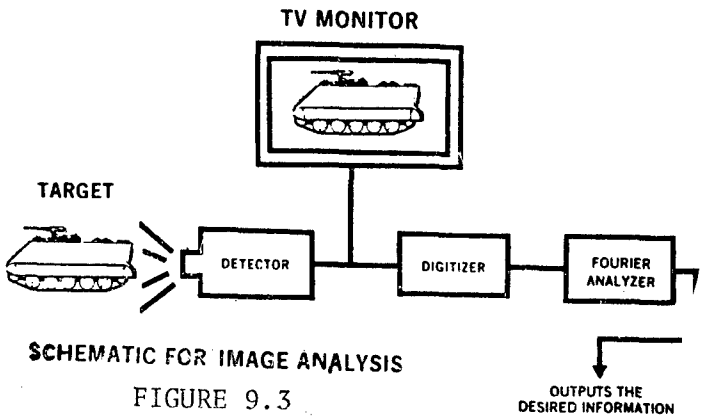

SCHEMATIC FOR IMAGE ANALYSIS

FIGURE 9.3

DIGITIZATION OF FRINGE PATTERN

FIGURE 9.4

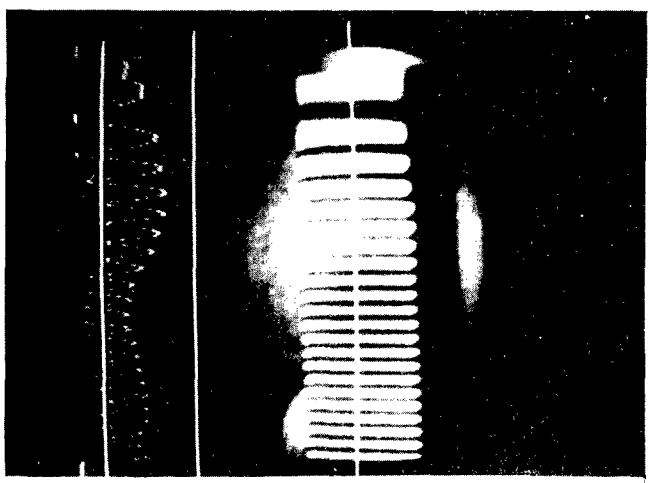

where A(t) is an additive function due to some slowly varying background effects and B(t) is essentially an envelope function. The magnitude of the Fourier Transform of the signal in Eq. 9.1 is displayed in Figure 9.6. The original time domain signal was sampled with a block size of 512 points. The frequency spectra in Figure 9.6 display the magnitudes of the 256 complex valved Fourier components. Since A(t) is relatively constant over the entire time domain signal, an elimination of the lowest frequency components should remove much of this additive term and all of the DC component. The two spectra in Figure 9.6 are the original and high pass filtered data which have been rescaled and plotted on one graph. The B(t) or AM modulated term represents a more difficult problem. Since B(t) $\cos\Delta\phi$ is a product function in the time domain, the frequency domain signal will consist of the convolution of the Fourier transforms of B(t) and $\cos\Delta\phi(t)$. These two spectra are effectively smeared together and no simple filter function can be constructed without knowing B(t) explicitly.

Figure 9.7 contains the inverse transform of the high pass filtered spectrum in Figure 9.6. The additive term A(t) and the modulation term B(t) are much smaller after this filtering operation. The DC or mean value of the signal is equal to zero so the zero crossing points are quite evident. The location of the dark fringe centers corresponds to the minimum intensity peaks while the location of the maximum intensity peaks corresponds to the centers of the bright fringes. The non-uniform fringe spacing increases from left to right and corresponds to a monotonically decreasing fringe separation distance as shown in Figure 9.1b.

The remaining AM modulation effects can be removed by analyzing either the positive and negative peaks or the zero crossings of the fringe data. The position of these points are first located and recorded using a computer algorithm. A listing of these points is shown in Figure 9.10. If the additive term A(t) in Eq. 9.1 is negligible, then the zero crossing data is exact since the product of B(t) $\cos\phi(t)$ is zero when only one of the functions is zero and is independent of the value of the other function. However, if A(t) is not negligible, then the zero crossings of the data will not necessarily correspond to times when $\cos\phi(t)$ is zero. The extremal points of the data are relatively independent of A(t) and B(t). The disadvantage of using the extremal points is that no distinct peak may exist.

The additive modulation terms were removed by inserting a positive or negative half period of a sine wave between two consecutive extremal points. The result is a pure frequency modulated (FM) signal with constant amplitude and variable spacing between consecutive extremal points. This signal is shown in Figure 9.11.

A comparison of the frequency spectra for the original and FM modified fringe data is illustrated in Figure 9.8. The "pure" FM modulated fringe data spectrum

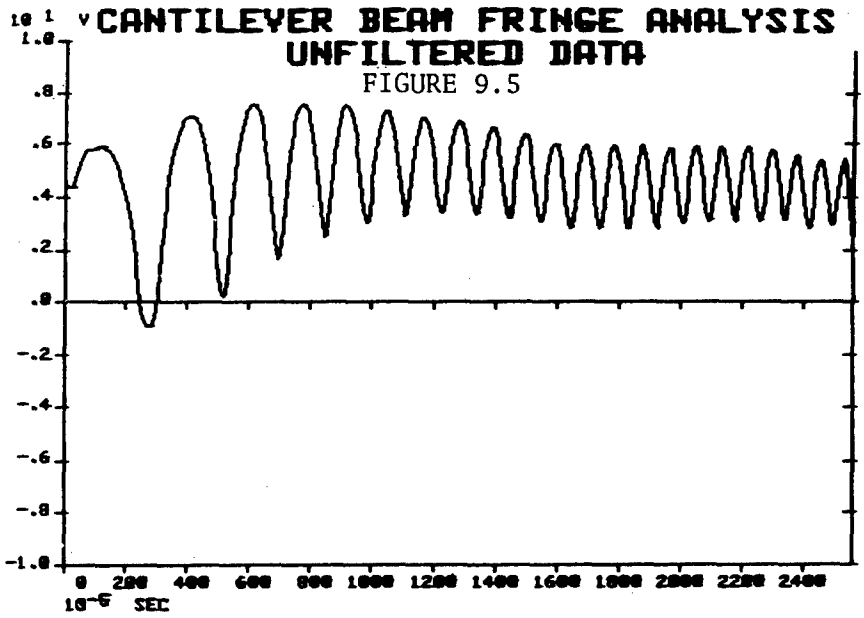

FIGURE 9.5

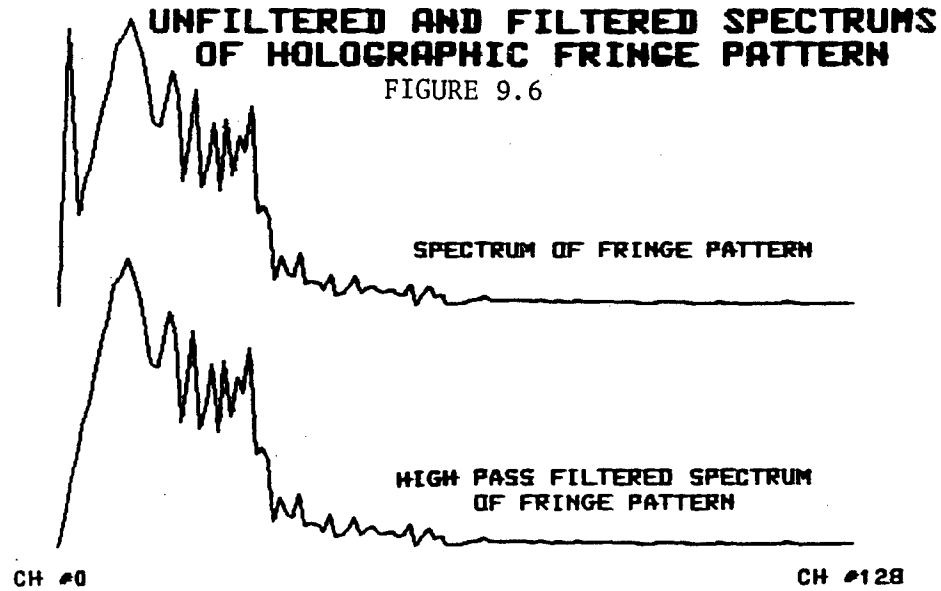

FIGURE 9.6

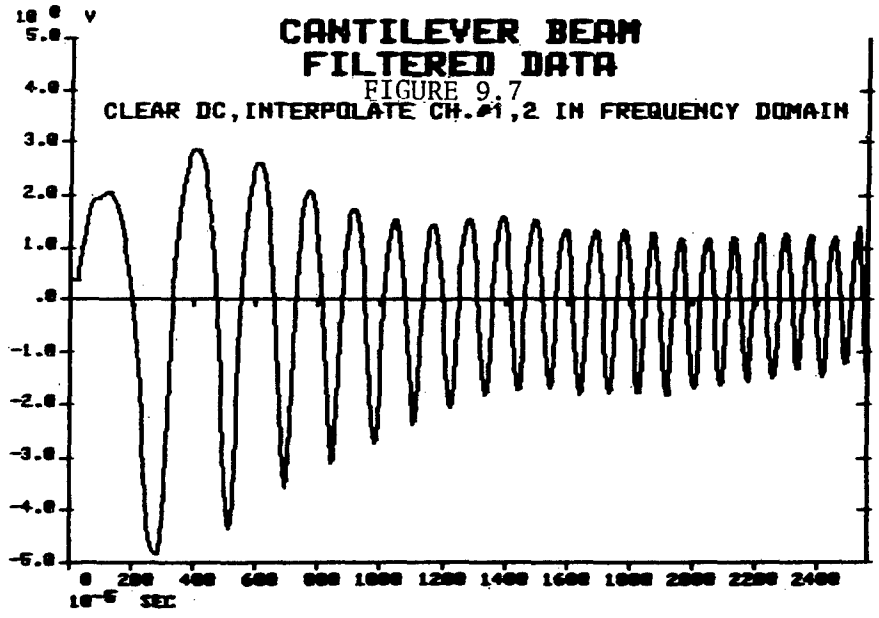

FIGURE 9.7

COMPARISON OF SPECTRA FOR UNFILTERED DATA AND PURE FM SIGNAL

FIGURE 9.8

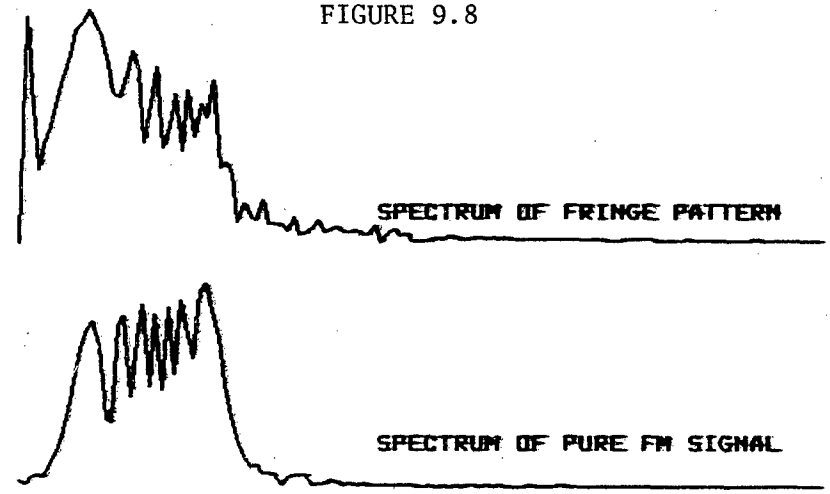

NOTE ATTENUATION OF LOWER FREQUENCIES

FRINGE SPACING

FRINGE NUMBER VS. DISTANCE

FUNCTION

FIGURE 9.9

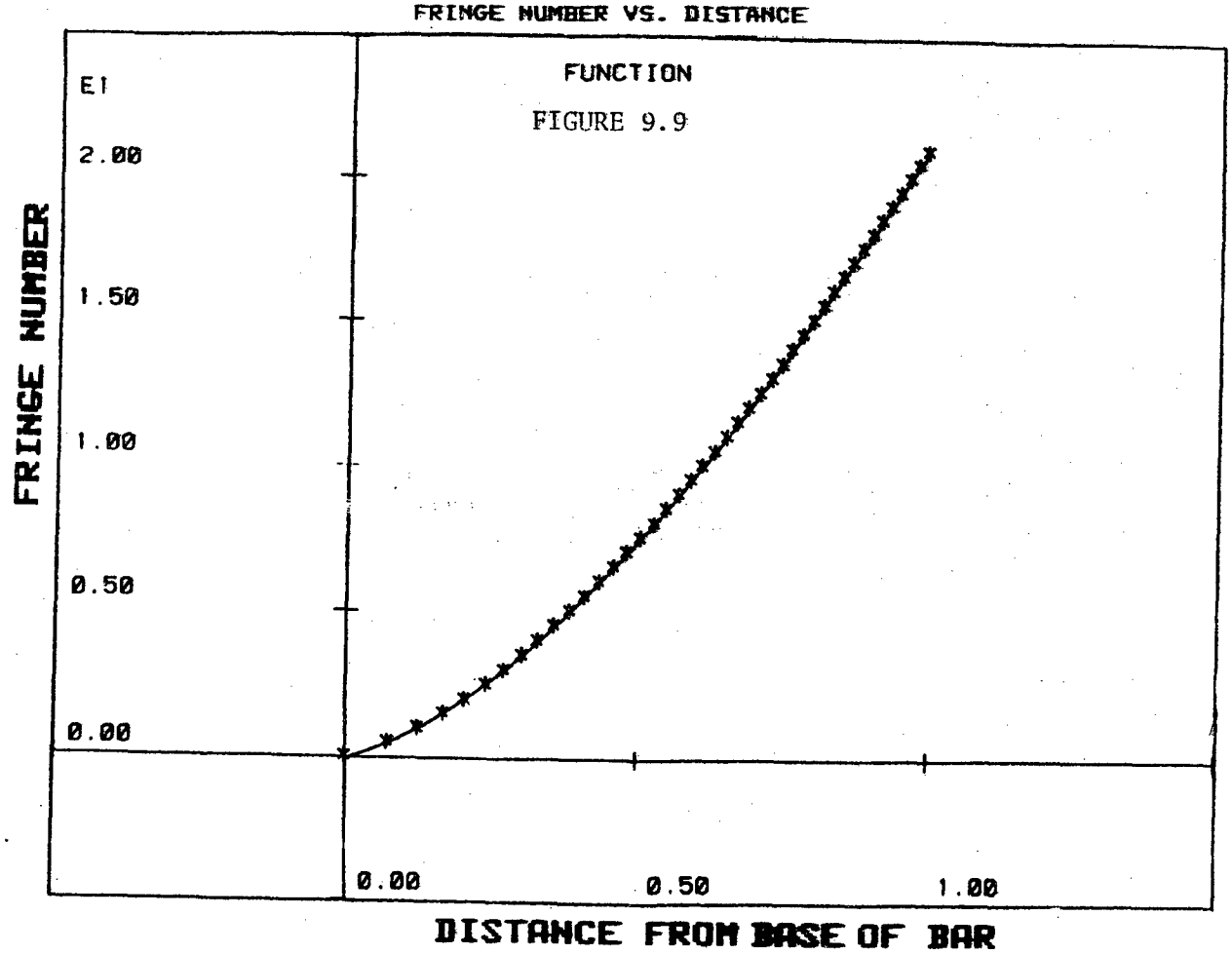

CANTILEVER BEAM
HOLOGRAPHIC FRINGE DATA

FIGURE 9.10

POSITIVE AND NEGATIVE PEAKS

DISTANCE	FRINGE ORDER
.0000	.0000
.0715	.5000
.1227	1.0000
.1676	1.5000
.2045	2.0000
.2413	2.5000
.2719	3.0000
.3026	3.5000
.3292	4.0000
.3578	4.5000
.3844	5.0000
.4090	5.5000
.4335	6.0000
.4580	6.5000
.4805	7.0000
.5030	7.5000
.5255	8.0000
.5460	8.5000
.5685	9.0000
.5889	9.5000
.6073	10.0000
.6278	10.5000
.6482	11.0000
.6666	11.5000
.6850	12.0000
.7055	12.5000
.7239	13.0000
.7423	13.5000
.7586	14.0000
.7771	14.5000
.7955	15.0000
.8118	15.5000
.8282	16.0000
.8466	16.5000
.8629	17.0000
.8793	17.5000
.8957	18.0000
.9120	18.5000
.9284	19.0000
.9447	19.5000
.9611	20.0000
.9754	20.5000
.9918	21.0000

ZERO CROSSINGS

STAN	FRINGE ORDER
.000	.0000
.040	.2500
.094	.7500
.151	1.2500
.184	1.7500
.226	2.2500
.255	2.7500
.290	3.2500
.316	3.7500
.347	4.2500
.3721	4.7500
.3987	5.2500
.4212	5.7500
.4478	6.2500
.4683	6.7500
.4948	7.2500
.5132	7.7500
.5378	8.2500
.5562	8.7500
.5807	9.2500
.5991	9.7500
.6196	10.2500
.6380	10.7500
.6584	11.2500
.6768	11.7500
.6973	12.2500
.7157	12.7500
.7341	13.2500
.7525	13.7500
.7689	14.2500
.7873	14.7500
.8036	15.2500
.8220	15.7500
.8384	16.2500
.8548	16.7500
.8732	17.2500
.8895	17.7500
.9059	18.2500
.9222	18.7500
.9386	19.2500
.9529	19.7500
.9693	20.2500
.9836	20.7500
1.0000	21.2500

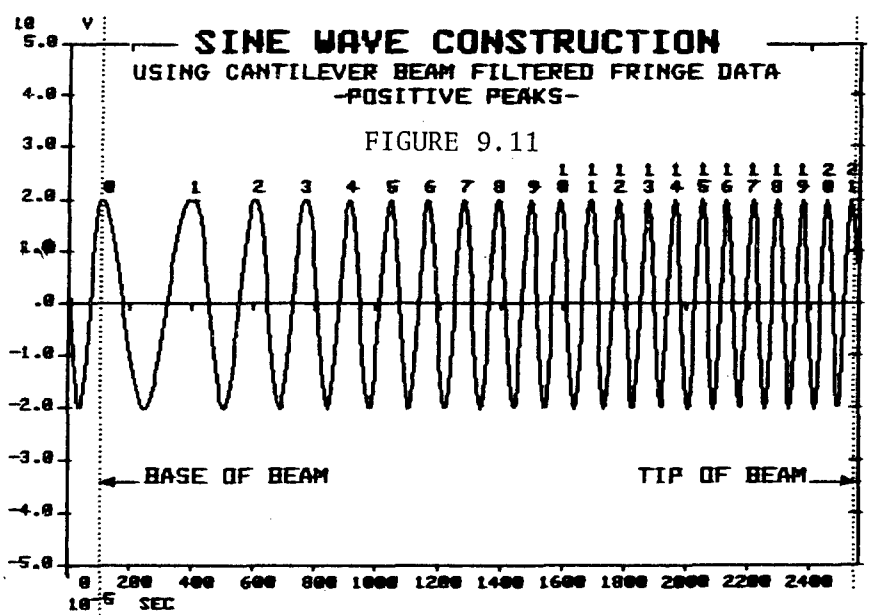

FIGURE 9.11

has more detail than the former. This result follows because the product of AM and FM modulated functions in the time domain corresponds to a convolution of the two functions in the frequency domain. The convolution operator smears the product spectra and removes much of the detailed resolution.

9.4 Data Analysis

Figure 9.9 contains a graph of the fringe order along the cantilever beam from the zero fringe position as a function of the distance of that particular fringe from the zero fringe position. The numerical values for the data points in Figure 9.9 are obtained from Figure 9.10. An equation for the smooth curve in Figure 9.9 is obtained by using a least squares estimate. The equation for the dimensionless cantilever deflection is illustrated in Figure 9.12. The polynomial coefficients for the least squares curve fit are also displayed for both the zero-crossing and positive/negative peak measurements. All distance measurements X/L are normalized relative to the length L of the cantilever beam. The three polynomial coefficients in Figure 9.12 are very nearly the same for either the zero-crossing or extremal point data. The ideal cantilever beam has an equation of the form

$$F(x) = N\lambda = d_o(3T^2 - T^3) \qquad 9.2$$

$$T = X/L$$

as found in Eq. 8.20. The linear term in Eq. 9.2 corresponds to a rotation of the beam about the clamping point or zero fringe position. The remaining discrepancies between the experimental and theoretical results is attributable to the non-ideal behavior of the metal beam.

EQUATION FOR CANTILEVER BEAM

$$F(X)=N\lambda=d(-T^3+3T^2)$$

WHERE $T=(X/L)$

CURVE OBTAINED

USING:
+/- PEAKS $F(X)=N\lambda=d(-4.65T^3+19.71T^2+6.22T)$

0 CROSSINGS $F(X)=N\lambda=d(-4.62T^3+19.72T^2+6.14T)$

FIGURE 9.12

d=DISPLACEMENT
X=DISTANCE ON BEAM FROM BASE
L=LENGTH OF BEAM

10. SUMMARY

Double exposure holograms have been taken of automotive components using a highly tuned ruby laser. Techniques are described for operating the laser and synchronizing the output relative to a vibrating object. Primary emphasis is placed upon the M151 utility truck. Excellent quality double exposure holograms reveal a great deal of local and global displacement amplitude information about the vibrating vehicle structure. A sequence of holograms is taken relative to the No. 1 spark plug pulse. These holograms are used to analyze engine displacement functions over an entire firing sequence. Additional holograms of the side door panels reveal the effects of the mechanical fastening upon the panel vibration behavior. This information is important for determining velocity profiles and the consequent acoustic power radiation from these panels.

Techniques are described for quantifying the fringe data in terms of the mechanical parameters for the structure. The density and contour of the holographic fringes are related to a surface displacement during the time interval between the pulses. The holographic fringe patterns are digitized and processed using a digital computer. The displacement of a cantilever beam is analyzed using these techniques. A good agreement is found between the experimental and theoretical results.

APPENDIX A

FRINGE FORMATION

The object surface consists of a collection of point scatterers. When an arbitrary point P undergoes a displacement $\vec{L}$ to a new position P', the holographic fringes result from the interference between the light which is scattered from P and P'. Figure A.1a illustrates the essential elements of the holographic recording system. The object is illuminated by a point source which is located at the origin O. Light is scattered by an object point P through the hologram to an observer at point Q. A double exposure hologram is recorded on a photographic plate, and between exposures point P is displaced by an amount $\vec{L}$. The observer Q who is looking at point P sees the displacement $\vec{L}$ produce an optical phase shift $\Delta\phi(x,y)$.

Several vectors are defined in Figure A.1b to determine the relationship between $\Delta\phi$ and $\vec{L}$. The vectors $\vec{R}$ and $\vec{r}_1$ lie in a plane which is defined by the points O,P,Q while $\vec{K}_1$ and $\vec{K}_2$ are propagation vectors for the light illuminating P and the light scattered toward the observer. The magnitude of the propagation vectors is $2\pi/\lambda$ and the phases of the two light rays which reach the observer are

$$\begin{aligned} \phi_1 &= \vec{K}_1 \cdot \vec{r}_1 + \vec{K}_2 \cdot (\vec{R} - \vec{r}_1) + \phi_r \\ \phi_2 &= \vec{K}_3 \cdot \vec{r}_3 + \vec{K}_4 \cdot (\vec{R} - \vec{r}_3) + \phi_r \end{aligned} \qquad \text{(A.1)}$$

The quantity ϕ_1 is the phase of the light which is scattered by P before displacement, ϕ_2 is the phase of the light which is scattered by P after displacement, and ϕ_r is the arbitrary phase which is assigned to these rays at the point source O. The phase difference $\Delta\phi$ which is measured by the observer Q is

$$\Delta\phi = \phi_2 - \phi_1 \ . \qquad \text{(A.2)}$$

The propagation vectors $\vec{K}_3$ and $\vec{K}_4$ are parallel to the observation directions after the displacement $\vec{L}$. The small changes $\Delta\vec{K}_1$ and $\Delta\vec{K}_2$ in the propagation vectors are given by

$$\begin{aligned} \vec{K}_3 &= \vec{K}_1 + \Delta\vec{K}_1 \\ \vec{K}_4 &= \vec{K}_2 + \Delta\vec{K}_2 \ . \end{aligned} \qquad \text{(A.3)}$$

The phase difference $\Delta\phi$ is given by

$$\Delta\phi = (\vec{K}_2-\vec{K}_1)\cdot(\vec{r}_1-\vec{r}_2) + \Delta\vec{K}_1\cdot\vec{r}_3 + \Delta\vec{K}_2\cdot(\vec{R}-\vec{r}_3). \qquad (A.4)$$

The magnitudes of $\vec{r}_1$ and $\vec{r}_2$ are usually much greater than $L = |\vec{r}_3-\vec{r}_1|$; consequently, the vectors $\Delta\vec{K}_1$ and $\Delta\vec{K}_2$ are perpendicular to $\vec{r}_3$ and $(\vec{R}-\vec{r}_3)$ respectively. Equation A.4 reduces to Equation A.5 for the configuration in Figure A.1b. These two scaler products vanish in Equation A.4 and $\Delta\phi$ becomes

$$\Delta\phi = (\vec{K}_2-\vec{K}_1)\cdot\vec{L} \qquad (A.5)$$

The sensitivity vector $\vec{K}$ is defined to be

$$\vec{K} = \vec{K}_2 - \vec{K}_1$$

$$\Delta\phi = \vec{K}\cdot\vec{L} \; . \qquad (A.6)$$

The approach for measuring a three dimensional displacement is now quite straight forward. Since a single observation yields one vector component of $\vec{L}$, three independent observations must be made to measure the three independent components of $\vec{L}$. Three holographic interferograms which are recorded along three independent orientations of the vector $\vec{K}_2$ can be used to obtain the necessary data. A system of three equations in three unknowns is used to uniquely determine the displacement vector $\vec{L}$.

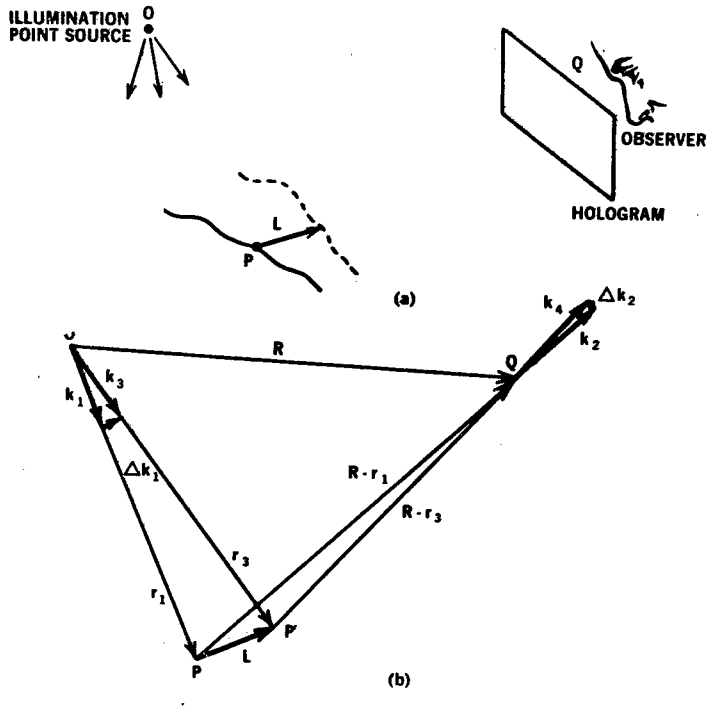

FIGURE A.1

Essential Elements of a Holographic Recording System

APPENDIX B

FRINGE LOCALIZATION

The fringes which one observes on a double exposure hologram of an object appear to be localized in space. These fringes may appear on the object surface or they may be localized in front or behind it. These latter fringes exhibit parallax as the observer shifts his viewing position.

The optical interference pattern occurs on the retina when a person views a double exposure hologram. The imaging system plays a very important role in forming the holographic fringes. The most important parameter is the aperture or entrance pupil which determines the solid angle of the ray cone that forms the image at each point in the image plane. A large aperture increases the resolution of the holographic fringes with a corresponding decrease in the depth of focus. The result is that fringes must be localized on or near the object surface for both to be in sharp focus. The small aperture increases the depth of field, but reduces the resolution and amount of light at the image plane.

A typical system is shown in Figure B-1 for viewing a double exposure hologram. A lens which focuses on a plane in front of the object surface images the composite optical field onto a detector surface. The interference pattern at Q' is identical to the one which is formed at Q by the same cone. The observer at Q' detects the light arriving in a ray cone which is centered on the axis PQQ' which has a solid angle that is determined by the aperture The ray cone emanates from the point Q and it is projected to the point Q'.

A pair of rays travel along each ray path - one each emanating from two images of the object. The pair of rays arrive at Q differing in phase by the amount $\Delta\phi$. The irradiance at Q is the sum of irradiances of all the ray pairs within the cone. The interference pattern near Q is the sum of all interference patterns due to motion of surface points within the cone. The value of $\Delta\phi$ varies significantly within the cone, and no holographic fringes are observed for a viewing system with large apertures near such points. A well defined average irradiance and fringe pattern exists near a point where the value $\Delta\phi$ is nearly constant within the cone. An observer finds that holographic fringes lie near a surface in space which is the locus of such points.

The localization of points Q with constant $\Delta\phi$ are determined by a variation of $\Delta\phi$ to minimize its value over a small cone of ray pairs. The condition of fringe localization is

$$d(\Delta\phi) = \partial_x(\Delta\phi)dx+\partial_y(\Delta\phi)dy = 0 \qquad (B.1)$$

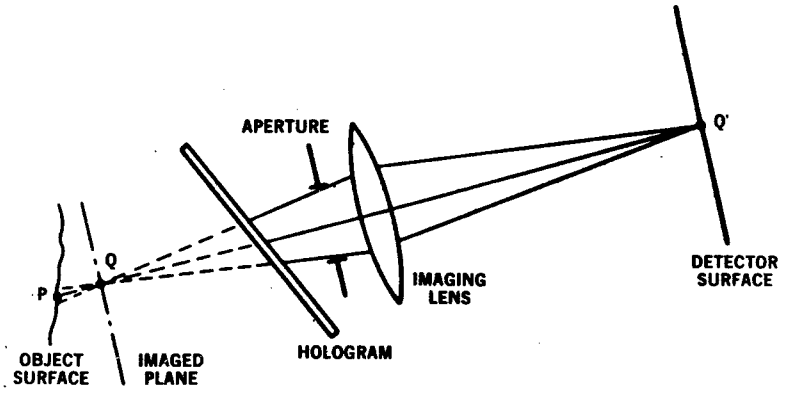

FIGURE B.1

A Simple Lens System for Optically Imaging Holographic Fringes

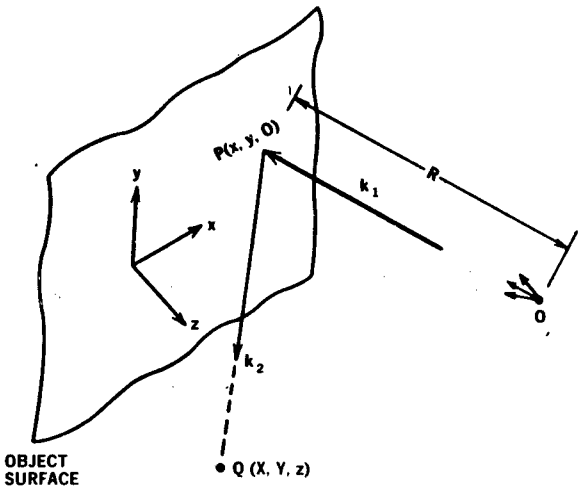

FIGURE B.2

Fringe Localization Coordinate Systems

where dx and dy are differential changes in the object which is viewed from the points Q (X,Y,Z). The quantity z is the distance from the surface to Q. The values of z define the surface of fringe localization as depicted in Fig. B.2.

The curvature of the illumination wavefront is quite small in most applications of holographic interferometry. The case of collimated object illumination affords considerable analytical simplification and it will be discussed in detail.

The expression for $\Delta\phi$ is given by Eq. B.2

$$\Delta\phi = 2\pi\vec{K}\cdot\vec{L}/\lambda\rho \tag{B.2}$$

where $\vec{K} = \vec{K}_2 - \vec{K}_1$ is a vector parallel to the sensitivity direction. The vector $\vec{K}_1$ is constant for collimated illumination while $\vec{K}_2$ and $\vec{L}$ are functions of the surface coordinates x, y and the observer position Q.

Equation B.1 for collimated illumination becomes:

$$(K_{2x}^{x} L_x + K_{2y}^{x} L_y + K_{2z}^{x} L_z + K_x L^{x}_{x} + K_y L^{x}_{y} + K_z L^{x}_{z}) \, dx$$

$$+ (K_{2x}^{y} L_x + K_{2y}^{y} L_y + K_{2z}^{y} L_z + K_x L^{y}_{x} + K_y L^{y}_{y} + K_z L^{y}_{z}) \, dy = 0 \tag{B.3}$$

where the superscript denotes partial differentiation with respect to either x or y (i.e. $\partial_y K_{2x} = K^{y}_{2x}$). Summation notation for Eq. B.3 is

$$\Sigma_{ij} (K^{i}_{2j} L_j + K_j L^{i}_{j}) \, dx^i = 0 \tag{B.4}$$

where the indices i, j are summed over the variables x, y and x, y, z respectively. Expressions for the derivatives of the components of $\vec{K}_2$ are obtained by geometrical considerations from Fig. B.2. The vector $\vec{K}_2$ always points from the object point P (x, y, o) to the fixed observation point Q (X,Y,Z). The distance PQ is devoted by ρ. The components of $\vec{K}_2$ are given as follows:

$$K_{2x} = (X - x)/\rho$$

$$K_{2y} = (Y - y)/\rho$$

$$K_{2z} = z/\rho$$

$$\rho = [(X - x)^2 + (Y - y)^2 + z^2]^{\frac{1}{2}}$$

The derivatives of k_{2j} are obtained from Eq. B.5 subject to the condition that

$$K_{2x}^2 + K_{2y}^2 + K_{2z}^2 = 1 \qquad \text{(B.6)}$$

The quantities K_{2j}^i are given as follows:

$$K_{2x}^x = -K_{2z}\,(K_{2y}^2 + K_{2z}^2)/z, \quad K_{2x}^y = K_{2z}\,K_{2x}\,K_{2y}$$

$$K_{2y}^x = K_{2z}\,K_{2x}\,K_{2y}\,/\,z \qquad K_{2y}^y = -K_{2z}\,(K_{2x}^2 + K_{2z}^2)/z \qquad \text{(B.7)}$$

$$K_{2z}^x = K_{2z}\,K_{2x}\,K_{2z}\,/\,z \qquad K_{2z}^y = K_{2z}\,K_{2y}\,K_{2z}\,/\,z.$$

The localization condition (Eq. B.4) yields after combining Eqs. B.5 and B.7.

$$\{K_{2z}\,[\,(K_{2y}^2 + K_{2z}^2)\,L_x - K_{2x}\,K_{2y}\,L_y - K_{2x}\,K_{2z}L_z\,]\,/\,z$$

$$- (K_x\,L_x^x + K_y\,L_y^x + K_z\,L_z^x)\}\,dx$$

$$+ \{K_{2z}\,[\,-K_{2x}\,K_{2y}\,L_x + (K_{2x}^2 + K_{2z}^2)\,L_y - K_{2y}\,K_{2z}\,L_z\,]/z \qquad \text{(B.8)}$$

$$- (K_x\,L_x^y + K_y\,L_y^y + K_z\,L_z^y)\}\quad dy = 0.$$

If the coefficients of dx and dy are varied independently, then each coefficient can be set equal to zero.

$$z = \frac{K_{2z}\,[(K_{2y}^2 + K_{2z})^2\,L_x - K_{2x}K_{2y}L_y - K_{2x}K_{2z}L_z\,]}{[K_xL_x^x + K_yL_y^x + K_zL_z^x\,]} \qquad \text{(B.9)}$$

$$z = \frac{K_{2z}\,[-K_{2x}\,K_{2y}\,L_x + (K_{2x}^2 + K_{2z}^2)\,L_y - K_{2y}K_{2z}\,L_z]}{(K_x\,L_x^y + K_y\,L_y^y + K_z\,L_z^y)}$$

Each of the equations B.9 generates a surface $z=z\,(x, y)$ in space when particular values are uniquely specified for $\vec{K}_1$, $\vec{K}_2$, and $\vec{L}$. Since both operations are satisfied simultaneously, the fringes are localized along a curve which is the intersection of the two surfaces.

References

1. K.A. Stetson and R.L. Powell, Interferometric Hologram Evaluation and Real-Time Vibration Analysis of Diffuse Objects, J. Opt Soc. Am, 55, 1694-1695 (1965).

2. R.K. Erf (Ed.), Holographic Nondestructive Testing, Academic Press, New York, 1974.

3. D.J. Monnier and K.D. Jones, Diesel-Engine Vibrations Measured with Holography, Laser Focus, December 1977.

4. A. Felske and A. Happe, Vibration Analysis by Double Pulsed Laser Holography, SAE Report #770030 (1977).

5. S.C. Gustafson, Pulsed Holographic Interferometry of Objects Subject to Both Uniform and Vibrational Motion, Optical Engineering/Nov-Dec (1980).

6. C.M. Vest, Holographic Interferometry, J.Wiley and Sons, New York, (1979).

14. DISTRIBUTION LIST

	No. of Copies
Deputy Undersecretary, Tactical Warfare Programs Office of Under Secretary for Research and Engineering ATTN: Mr. David C. Hardison The Pentagon, Room 3E-1044 Washington, D.C. 20301	1
Director, Land Warfare Office of Undersecretary for Research and Engineering ATTN: Mr. Charles Bernard The Pentagon, Room 3E-1025 Washington, D.C. 20301	1
Office, Secretary of the Army Undersecretary, SAUS ATTN: Mr. J. R. Ambrose The Pentagon, Room 3E-732 Washington, D.C. 20310	1
LTG James H. Merryman Deputy Chief of Staff for Research, Development and Acquisition ATTN: DAMA-ZA The Pentagon, Room 3E-412 Washington, D.C. 20310	1
Office of the Deputy Chief of Staff for Research, Development and Acquisition Advisor/RDA Analysis ATTN: DAMA-ZA, Mr. Hunter Woodall The Pentagon, Room 3E-411 Washington, D.C. 20310	1
MG James P. Malorey Director, Weapons Systems Office of the Deputy Chief of Staff for Research, Development and Acquisition ATTN: DAMA-WS The Pentagon, Room 3E-448 Washington, D.C. 20310	1

	No. of Copies
Director, Advanced Concepts Team Office of the Deputy Chief of Staff for Research, Development and Acquisition ATTN: DAMA-ZE, Dr. C. H. Church The Pentagon, Room 3E-363 Washington, D.C. 20310	1
Director, Army Research Office of the Deputy Chief of Staff for Research, Development and Acquisition ATTN: DAMA-AR, Dr. M.E. Lasser The Pentagon, Room 3E-360 Washington, D.C. 20310	1
Chief, Ground Combat Systems Office of the Deputy Chief of Staff for Research, Development and Acquisition ATTN: DAMA-WSW, LTC A. T. Crumpton The Pentagon, Room 3C-464 Washington, D.C. 20310	1
Chief, Ground Combat Sytems Office of the Deputy Chief of Staff for Research, Development and Acquisition ATTN: DAMA-WSW, LTC W. L. Ivey The Pentagon, Room 3D-455 Washington, D.C. 20310	1
GEN Donald R. Keith, Commanding General US Army Materiel Development and Readiness Command ATTN: DRCCG 5001 Eisenhower Ave. Alexandria, VA 22333	1
MG O. B. Gonzales, Director/Dev, Eng & Acq US Army Materiel Development and Readiness Command ATTN: DRCDE 5001 Eisenhower Ave. Alexandria, VA 22333	1

	No. of Copies
Commander US Army Materiel Development and Readiness Command ATTN: DRCDMD-ST, Dr. R. L. Haley Asst Deputy/Science and Technology 5001 Eisenhower Ave. Alexandria, VA 22333	1
MG O. C. Decker, Commander US Army Tank-Automotive Command ATTN: DRSTA-CG Warren, MI 48090	1
BG C. M. Matthews, Deputy Commander for Research and Development Center US Army Tank-Automotive Command ATTN: DRSTA-NG Warren, MI 48090	1
Commander US Army Tank-Automotive Command ATTN: DRSTA-NS, Dr. E. N. Petrick Technical Director, R&D Center Warren, MI 48090	1
Commander US Army Tank-Automotive Command ATTN: DRSTA-Z, COL T. H. Huber Director, Tank-Automotive Concepts Laboratory Warren, MI 48090	1
Commander US Army Tank-Automotive Command ATTN: DRSTA-ZE, Mr. J. B. Gilvydis Exploratory Dev Div Warren, MI 48090	1
Commander US Army Tank-Automotive Command ATTN: DRSTA-R, COL H. H. Dobbs Director, Tank-Automotive Systems Laboratory Warren, MI 48090	1

	No. of Copies
Commander US Army Tank-Automotive Command ATTN: DRSTA-RG, Mr. Edward Hamparian Chief, Propulsion Sys Div, TASL Warren, MI 48090	1
Commander US Army Tank-Automotive Command ATTN: DRSTA-TSL Warren, MI 48090	2
Commander US Army Tank-Automotive Command Tank Development Office ATTN: DRSTA-NU, COL J. Wasson Warren, MI 48090	1
Commander US Army Tank-Automotive Command Develpment Project Office/Vehicle NBC ATTN: DRSTA-NR, LTC P. Brake Warren, MI 48090	1
MG D. Ball, Project Manager M1 Tank System ATTN: DRCPM-GCM Warren, MI 48090	1
Program Manager M1 Tank System ATTN: DRCPM-GCM-SA, Mr. J. Roossien Warren, MI 48090	1
BG D. Whalen, Project Manager Fighting Vehicle Systems ATTN: DRCPM-FVS Warren, MI 48090	1
Project Manager M60 Tanks ATTN: DRCPM-M60, Mr. F. Pradko Warren, MI 48090	1

	No. of Copies
Project Manager Improved TOW Vehicle ATTN: DRCPM-ITV, COL J. A. Chernault Warren, MI 48090	1
Project Manager Armored Combat Vehicle Technology ATTN: DRCPM-CVT, LTC J. B. Welsh Warren, MI 48090	1
Commander US Army Armament Research and Development Command ATTN: DRDAR-LCW, Mr. H. L. Garver Director, Weapons Division Dover, NJ 07801	1
Director US Army ARRADCOM Benet Weapons Laboratory ATTN: DRDAR-LCB-D, Dr. John Zweig Chief, Dev Engineering Branch Watervliet, NY 12189	1
Director Balistic Research Laboratory ATTN: DRDAR-BL, Dr. R. J. Eichelberger Aberdeen Proving Grounds, MD 21005	1
Director US Army Materials and Mechanics Research Center ATTN: DRXMR-X, Dr. E.S. Wright Watertown, MA 02171	1
Commander US Army Natick Research and Developmennt Command ATTN: DRDNA-ZT, COL G. R. Rubin Natick, MA 01760	1

	No. of Copies
Director Defense Advanced Research Projects Agency ATTN: Defense Sciences Office Dr. E. Levinthal 1400 Wilson Boulevard Arlington, VA 22209	1
Director Defense Advanced Research Projects Agency ATTN: Material Sciences Division Dr. R. Gogolewski 1400 Wilson Boulevard Arlington, VA 22209	1
Deputy Director of Technology Defense Advanced Research Projects Agency ATTN: Mr. Lawrence Lynn 1400 Wilson Boulevard Washington, D.C. 22209	1
Director Human Engineering Laboratory ATTN: DRXHE-CCD, Mr. A. Eckles Aberdeen Proving Grounds, MD 21005	1
Commander US Army Communications Research and Development Command ATTN: DRDCO-TD Fort Monmouth, NJ 07703	1
Commander US Army Electronics Research and Development Command Technical Support Activity ATTN: DELSD-L Fort Monmouth, NJ 07703	1
Commander/Director Combat Surveillance and Target Acquisition Laboratory ATTN: DELCS-D Fort Monmouth, NJ 07703	1

	No. of Copies
Commander Harry Diamond Laboratories ATTN: DELHD-TD 2800 Powder Mill Road Adelphi, MD 20783	1
Director Night Vision and Electro-Opitcs Laboratory ATTN: DELNV-SI (Systems Integration) Fort Belvoir, VA 22060	1
Commander US Army Mobility Equipment Research & Development Command ATTN: DRDME-WC (Tech Library) Fort Belvoir, VA 22060	1
Commander US Army Armament Material Readiness Command ATTN: DRSAR-LEP-L, Tech Library Rock Island, IL 61299	1
Commander US Army Combat Developments Experimentation Command ATTN: Technical Library Fort Ord, CA 93941	1
Commander US Army Training and Doctrine Command ATTN: ATZL-MT, MAJ W. Jones Fort Monroe, VC 23351	3
Director US Army TRADOC System Analysis Activity ATTN: ATAA-SL, Tech Library White Sands Missile Range, NM 88002	1
Commander US Army Armor Center ATTN: ATZK-CG Fort Knox, KY 40121	1

	No. of Copies
Commandant US Army Armor School ATTN: ATSB-DAD Fort Knox, KY 40121	1
President US Armor and Engineer Board ATTN: ATZK-AE-PD, COL L. Fleming Fort Knox, KY 40121	1
Commander US Army Infantry Center ATTN: ATSH-CD, LTC Wilson Fort Benning, GA 31905	1
Commander Defense Technical Information Center ATTN: DDC Cameron Station Alexandria, VA 22314	15
Commander US Army Research Office ATTN: DRXRO-ZC P.O. Box 12211 Research Triangle Park, NC 27709	1
Director Institute for Defense Analysis ATTN: Documents Library 400 Army-Navy Drive Arlington, VA 22202	1
Commander US Army Research Instititue ATTN: PERI-SF 5001 Eisenhower Avenue Alexandria, VA 22333	1
Commandant US Military Academy ATTN: USMA Library West Point, NY 10996	1

	No. of Copies
Office of the Dean of the Academic Board Department of Engineering ATTN: MADN-F, CPT Hoppy Prof of Weapons Sys Eng West Point, NY 10996	1
Industrial College of the Armed Forces Military Faculty ATTN: ICFA-EA, LTC F. Y. Hartline Washington, D.C. 20319	1
Superintendent US Naval Postgraduate School ATTN: Tech Rpts Sec Monterey, CA 93940	1
Director Naval Ships R&D Center ATTN: Code 1129, Mr. E. Wolfe Bethesda, MD 20084	1
Commander US Army Foreign Science & Tech Center ATTN: DRXST-CE Charlottesville, VA 22902	1
Commander US Army Missile Command ATTN: DRSMI-YM Redstone Arsenal, AL 35898	1
Commander US Army Armament Materiel Readiness Command ATTN: DRSAR-ASB Rock Island, IL 61299	1
Commander US Army Armament Research and Develoment Command ATTN: DRDAR-RAI Dover, NJ 07801	1

	No. of Copies
Commander US Army Armament Research and Development Command ATTN: DRDAR-RAI-B Aberdeen Proving Ground, MD 21005	1
Commander US Army Armanent Research and Development Command ATTN: DRDAR-RAI-W Waterveilt, NY 12189	1
Commander US Army Aviation Research and Development Command ATTN: DRDAV-ED 4300 Goodfellow Blvd St. Louis, MO 63120	1
Director US Army Research and Technical Laboratories ATTN: DAVDL-FIO AMES Research Center Moffet Field, CA 94035	1
Commander US Army Materiel Development and Readiness Command ATTN: DRCDE-FIO 5001 Eisenhower Avenue Alexandria, VA 22333	1
Commander US Army Electronics Research and Development Command ATTN: DRDEL-FI-M Ft. Monmouth, NJ 07703	1
Director Office of Missile Electronic Warfare US Army Electronic Warfare Laboratory ATTN: DELEW-M-FM White Sands Missile Range, NM 88002	1

	No. of Copies
Director US Army Materials and Mechanics Research Center ATTN: DRXMR-XFI Watertown, MA 02171	1
Director US Army Materiel Systems Analysis Activity ATTN: DRXSY-PF Aberdeen Proving Ground, MD 21005	1
Commander US Army Missile Command ATTN: DRSMI-XF Redstone Arsenal, AL 35898	1
Commander US Army Mobility Equipment Research and Development Command ATTN: DRDME-UY Ft. Belvoir, VA 22060	1
Commander US Army Natick Research and Development Laboratories ATTN: DRDNA-TI Natick, MA 01760	1
Commander US Army Tank-Automotive Command ATTN: DRSTA-NF Warren, MI 48090	5
Commander US Army Test and Evaluation Command ATTN: DRSTE-TO-F Aberdeen Proving Ground, MD 21005	1
Commander Dugway Proving Ground ATTN: STEDP-PO-FI Dugway, UT 84022	1

	No. of Copies
Commander US Army Electronic Proving Ground ATTN: STEEP-MM-IS Ft. Huachuca, AZ 85613	1
Commander US Army White Sands Missile Range ATTN: STEWS-TE-F White Sands Missile Range, NM 88002	1
Commander US Army Yuma Proving Ground ATTN: STEYP-FIO Yuma, AZ 85364	1
Commander US Army Training and Doctrine Command ATTN: ATDO-T Ft. Monroe, VA 23651	1
HQ Department of the Army ATTN: DAMI-FIT Washington, D.C. 20310	1
Teledyne Continental Motors General Products Division ATTN: Mr. Wade Kingsbury 76 Getty Street Muskegon, MI 49442	1
FMC Corporation Western Administrative Offices ATTN: Mr. Robert Cole 1105 Coleman Avenue, Box 760 San Jose, CA 95106	1
General Dynamics Land Systems Division ATTN: Mr. J. Yeats 15999 Lawrence Avenue Centerline, MI 48015	1